Vertical Structure and Transient Behavior of Convective–Stratiform Heating in TOGA COARE from Combined Satellite–Sounding Analysis

SONG YANG AND ERIC A. SMITH

Department of Meteorology, The Florida State University, Tallahassee, Florida

(Manuscript received 5 November 1998, in final form 26 August 1999)

ABSTRACT

Datasets of daily high-resolution upper-air soundings and Special Sensor Microwave/Imager (SSM/I) passive microwave measurements from the Tropical Ocean and Global Atmosphere Coupled Ocean–Atmosphere Response Experiment (TOGA COARE) intensive operation period are used for large-scale diagnostic budget calculations of the apparent heat source (Q_1), the apparent moisture sink (Q_2), and latent heating to investigate the mechanisms of diabatic heating and moistening processes within the TOGA COARE Intensive Flux Array (IFA). Latent-heating retrievals are obtained from The Florida State University SSM/I-based precipitation profile retrieval algorithm. The estimates are correlated well with heating calculations from the soundings in which approximately 70% of the total heating arises from latent heat release. Moisture-budget processes also have a strong relationship with the large-scale environment, in which drying from condensation is mainly balanced by large-scale horizontal convergence of moisture flux. It is found that there may be more convective activity in summer than in winter over the tropical region of the western Pacific Ocean. Results also show that Q_1 and Q_2 exhibit a 20–30-day oscillation, in which active periods are associated with strong convection.

Comparisons of the Q_1–Q_2 calculations over IFA are made with a number of previously published results to help to establish the similarities and differences of Q_1–Q_2 between the warm pool and other regions of the Tropics. The Q_1–Q_2 budget analyses over IFA then are used to study quantitatively the detailed vertical heating structures. Cumulus-scale heating–moistening processes are obtained by using published radiative divergence (Q_R) data, retrieved latent heating, and the Q_1–Q_2 calculations. These results show that cumulus-scale turbulent transport is an important mechanism in both heat and moisture budgets. Although daily estimates of eddy vertical moisture flux divergence are noisy, by averaging over 7-day periods and vertically integrating to obtain surface latent heat flux, good agreement with measured surface evaporation is found. This agreement demonstrates the feasibility of estimating averaged eddy heat–moisture flux profiles by combining satellite-derived rain profile retrievals with large-scale sounding and Q_R data, a methodology that helps to shed light on the role of cumulus convection in atmospheric heating and moistening.

1. Introduction

The role of deep cumulus clouds in the heat balance of the tropical atmosphere first was investigated by Riehl and Malkus (1958). Palmén and Riehl (1957) and Miller (1962) indicated that latent heat release from cumulus clouds provides the main source of energy for the heat budget of a tropical cyclone, which largely is maintained as a balance between outflow of energy and internal latent heating from the condensation–precipitation process. Yanai et al. (1973) described the role of cumulus convection in the heating and moistening of such cloud systems.

The vertical heating profile resulting from convection provides the link between regional-scale and planetary-scale weather systems. For example, the planetary-scale tropical circulation and the interaction process between Tropics and higher latitudes respond differently to different heating profiles (Hartmann et al. 1984). Various studies (e.g., Johnson 1976; Thompson et al. 1979; Esbensen and Wang 1988; Frank and McBride 1989; McBride and Holland 1989; Gallus and Johnson 1991) have provided calculations of the apparent heat source (Q_1) and apparent moisture sink (Q_2) for special cases by applying the method of Yanai et al. (1973). Their results show that heating structures vary with weather systems and their locations. Lau and Peng (1987) found that different shapes of the vertical heating profile will lead to different phase speeds of excited Kelvin waves. Wu et al. (1993) showed that external heating effects (forced from outside tropical ocean areas) play an important role in triggering El Niño–Southern Oscillation (ENSO) variability. These results suggest that more accurate vertical diabatic heating profiles would improve model simulations, likely leading to further understand-

Corresponding author address: Eric A. Smith, Global Hydrology and Climate Center, NASA–UAH, 977 Explorer Blvd., Huntsville, AL 35806.
E-mail: eric.smith@msfc.nasa.gov

ing of the general circulation and the cause of ENSO variations.

The Tropical Ocean and Global Atmosphere Coupled Ocean–Atmosphere Response Experiment (TOGA COARE) is the most recent field experiment that provides research-quality datasets covering the west Pacific Ocean warm pool. Studies based on these datasets are improving understanding about heating and moistening processes over the warm-pool environment. For example, Frank and Wang (1996) investigated surface heat and moisture fluxes, Q_1 profiles, and surface rainfall estimated from Q_1 and Q_2 analyses over seven different configuration arrays during the TOGA COARE intensive operation period (IOP). Their results show that the Q_1 profiles generally are consistent among these arrays, except that the maximum heating was located at a higher level over the land arrays. Lin and Johnson (1996) also studied heating and moistening processes over the warm pool during TOGA COARE, finding that the IOP-averaged Q_1 profile shows positive heating at all levels of the troposphere with peak heating between 400 and 450 hPa.

None of the recent studies of time variations in the Q_1 and Q_2 budgets have investigated the difference between convective and stratiform situations. In addition, little knowledge has been forthcoming concerning the contribution of cumulus-scale turbulence to heating and moistening, especially over oceans. This lack of knowledge mostly is from a lack of vertical rain-rate measurements and high-density observations from radiosonde networks. Moreover, given the uncertainties in conventional surface precipitation measurements, progress on the detailed aspects of tropical–oceanic cumulus-scale heat–moisture budgets is difficult to pursue.

Satellite infrared (IR) and passive microwave (PMW) measurements fortunately can supply information needed for retrieving precipitation and latent heating profiles (e.g., Adler et al. 1993; Wilheit et al. 1994; Smith et al. 1998). Wilheit et al. (1994) and Smith et al. (1998) emphasized how physically based approaches for retrieving precipitation over oceans can be conducted with PMW algorithms. Physically based PMW inversion methods, such as those developed at The Florida State University (FSU) and the National Aeronautics and Space Administration (NASA) Goddard Space Flight Center, which retrieve vertical distributions of hydrometeors through inversion of Special Sensor Microwave Imager (SSM/I) measurements (e.g., Kummerow and Giglio 1994a,b; Smith et al. 1994a,b,c,d; Kummerow et al. 1996), have advantages over the surface rain-map-type algorithms, because they provide vertical profiles of both rain rate and latent heating (Yang and Smith 1999a).

Based on TOGA COARE Intensive Flux Array (IFA) datasets, Yang and Smith (1999a,b) have shown that retrieved surface rain rates from SSM/I are consistent with rain rates obtained from shipboard radars in terms of rain-rate magnitude, horizontal distribution, and temporal variation. They evaluated the accuracy of latent heating profiles estimated from the vertical derivative mass flux approach, recalibrated with a rain-rate-category scheme tied to surface rainfall from the radar measurements. These results indicate that the uncertainty in retrieved daily latent heating would be about 20%. The large-scale time–space distributions of monthly mean latent heating retrieved from SSM/I measurements reveal that the locations of significant latent heating are consistent with well-known large-scale cloud systems, especially the ITCZ, South Pacific Convergence Zone (SPCZ), monsoon circulation, and extratropical storm tracks (Yang and Smith 1999b). In addition, Yang and Smith (1999a) estimated the vertical eddy moisture flux from the residuals between the Q_2 budget and SSM/I-derived latent heating for a 17-day optimal TOGA COARE IOP sounding dataset. A comparison of the smoothed estimated surface evaporation with independently measured surface evaporation over IFA shows similar magnitudes, with a 0.55 correlation coefficient.

In this paper, the method tested by Yang and Smith (1999a) is extended to the entire TOGA COARE IOP dataset for a comprehensive investigation of the Q_1 and Q_2 budgets, their time variability, their differences with respect to embedded convective–stratiform systems, and contributions by vertical eddy fluxes of heating and moistening. The aim of this study is to shed light on the mechanisms of tropical heating and moistening and the role of cumulus-scale turbulence in tropical convective and stratiform systems. It also is noted that this approach can be helpful in the development of cloud parameterization schemes.

2. Methodology

Averaging the thermodynamic energy and moisture equations over a horizontal area yields the following expressions for Q_1 and Q_2 (e.g., see Yanai et al. 1973):

$$Q_1 \equiv \frac{\partial \overline{s}}{\partial t} + \overline{\nabla \cdot s\mathbf{V}} + \frac{\partial \overline{s}\,\overline{\omega}}{\partial p}$$
$$= L_v(\overline{c} - \overline{e}) - Q_R - \frac{\partial \overline{s'\omega'}}{\partial p} \quad \text{and} \qquad (1)$$

$$Q_2 \equiv -L_v\left(\frac{\partial \overline{q}}{\partial t} + \overline{\nabla \cdot q\mathbf{V}} + \frac{\partial \overline{q}\,\overline{\omega}}{\partial p}\right)$$
$$= L_v(\overline{c} - \overline{e}) + L_v\frac{\partial \overline{q'\omega'}}{\partial p}, \qquad (2)$$

where t is the time coordinate, s is the dry static energy ($c_pT + gz$), c_p is the specific heat of air at constant pressure, T is the temperature, g is the acceleration of gravity, z is the geopotential height, p is the pressure, q is the mixing ratio of water vapor, $\mathbf{V}$ is the horizontal wind vector, ω is the vertical p velocity, L_v is the latent heat of condensation, c is the rate of condensation per unit mass of air, e is the associated rate of evaporation,

and Q_R is the radiative cooling rate. The overbar denotes the IFA horizontal average, and the prime denotes the deviation from the average caused by unresolved eddies such as cumulus-scale convection and turbulence. Therefore, Q_1 is made up of radiative cooling, net latent heat release, and the vertical convergence of the vertical eddy transport of sensible heat, whereas Q_2 consists of net condensation and the vertical divergence of the vertical eddy transport of moisture. The techniques used for calculation of Q_1 and Q_2 are described in Yang and Smith (1999a).

Integrating Eqs. (1) and (2) from the tropopause (p_t) to the surface (p_s) yields:

$$\langle Q_1 \rangle = L_v P + S - \langle Q_R \rangle \quad \text{and} \tag{3}$$

$$\langle Q_2 \rangle = L_v P - L_v E, \tag{4}$$

where

$$\langle\ \rangle = \frac{1}{g}\int_{p_t}^{p_s} (\ )\, dp \tag{5}$$

and P, S, and E are the surface precipitation rate, the surface sensible heat flux, and the surface evaporation rate per unit area, respectively.

The surface sensible and latent heat fluxes can be estimated from the bulk transfer formulas

$$S = \rho_a c_p \overline{V}_s C_H (\overline{T}_s - \overline{T}_a) \quad \text{and} \tag{6}$$

$$L_v E = \rho_a L_v \overline{V}_s C_E (\overline{q}_s - \overline{q}_a), \tag{7}$$

where the overbar has the same meaning as defined previously. In these equations, ρ_a is air density, $\overline{V}_s$ is mean surface wind speed, and the subscripted $\overline{T}$ – $\overline{q}$ quantities are mean temperature and specific humidity at reference height (subscript a) and sea surface (subscript s). The C_H and C_E factors are semiempirically derived bulk transfer coefficients, which are crucial to the method. Because environmental conditions for the in-depth study of Bradley et al. (1991) were similar to those of the TOGA COARE IFA, the C_H and C_E factors from that study have been used for this analysis.

Initial latent heating profiles are estimated by evaluating the vertical derivatives of retrieved liquid–ice water mass fluxes that are proportional to condensation and deposition heating fluxes along the height axis. A detailed description of the FSU precipitation profile retrieval algorithm is given in Smith et al. (1994a) and Yang and Smith (1999a). The components of latent heating from raindrops ($Q_{\rm rd}$), ice particles ($Q_{\rm ip}$), and cloud drops ($Q_{\rm cd}$) at a discrete vertical index i are obtained by the following expressions:

$$Q_{\rm rd}(i) = \frac{gL_v}{2c_p}\{[W_{\rm rd}(i+1) + W_{\rm rd}(i)] - [W(i+1) + W(i)]\} \times \left[\frac{\mathrm{LWC}_{\rm rd}(i+1) - \mathrm{LWC}_{\rm rd}(i)}{p(i+1) - p(i)}\right], \tag{8}$$

$$Q_{\rm ip}(i) = \frac{g(\delta_{1,j}L_v + L_f)}{2c_p} \times \{[W_{\rm ip}(i+1) + W_{\rm ip}(i)] - [W(i+1) + W(i)]\} \times \left[\frac{\mathrm{LWC}_{\rm ip}(i+1) - \mathrm{LWC}_{\rm ip}(i)}{p(i+1) - p(i)}\right], \tag{9}$$

and

$$Q_{\rm cd}(i) = -\frac{gL_v}{2c_p}[W(i+1) + W(i)] \times \left[\frac{\mathrm{LWC}_{\rm cd}(i+1) - \mathrm{LWC}_{\rm cd}(i)}{p(i+1) - p(i)}\right], \tag{10}$$

where L_v and L_f are the latent heats of vaporization and fusion, c_p is isobaric specific heat, and $\mathrm{LWC}_{\rm rd}$, $\mathrm{LWC}_{\rm ip}$, and $\mathrm{LWC}_{\rm cd}$ are the equivalent liquid water contents of raindrops, graupel particles, and cloud drops, respectively. Note that δ is the Dirac–delta function with j taken as 1 when the heating from deposition is above the level of maximum $\mathrm{LWC}_{\rm ip}$ but as 0 below the maximum where only a melting process can be considered (i.e., where deposition is not valid thermodynamically). Note that the maximum $\mathrm{LWC}_{\rm ip}$ level is taken as the effective melting level, $W(i)$ is the cloud-scale vertical velocity that is regressed from hydrometeor profiles, and $W_{\rm rd}(i)$ and $W_{\rm ip}(i)$ are the mean terminal velocities for raindrops and graupel particles. Based on approximations given in Pruppacher and Klett (1980) and Böhm (1989), the $W_{\rm rd}$ and $W_{\rm ip}$ terms are given by

$$W_{\rm rd} = \frac{\mathrm{Re}_{\rm rd}\eta}{\rho_a \overline{d}_{\rm rd}} \quad \text{and} \tag{11}$$

$$W_{\rm ip} = \frac{\mathrm{Re}_{\rm ip}\eta}{\rho_a \overline{d}_{\rm ip}}, \tag{12}$$

where $\mathrm{Re}_{\rm rd}$ and $\mathrm{Re}_{\rm ip}$ are the characteristic Reynolds numbers, $\overline{d}_{\rm rd}$ and $\overline{d}_{\rm ip}$ are the mean diameters of raindrops and graupel particles, and η is the dynamic viscosity of air. The method to estimate the mean diameters of raindrops and graupel particles is based on the assumption that these length scales are proportional to their associated LWC magnitudes. A description of the calculation procedure is given in the appendix.

Total latent heating is obtained by summing the heating terms from liquid and ice precipitation and cloud water mass flux from vertical motion within the cloud. This initial estimate of latent heating then is adjusted according to a calibration procedure that requires that the ensemble vertical integral of total latent heating over the TOGA COARE IOP equal the ensemble heating associated with surface precipitation as determined by the TOGA COARE shipboard radars. The calibration scheme is discussed in detail in Yang and Smith (1999a).

After determination of Q_1 and Q_2 from the large-scale diagnostic budget analysis and the latent heating from

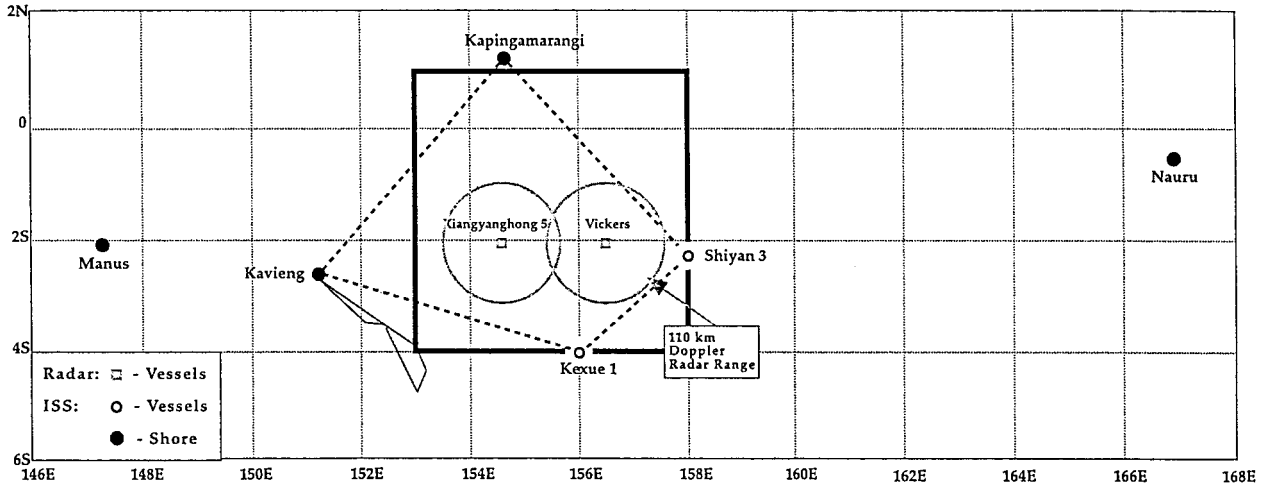

FIG. 1. Schematic diagram of TOGA COARE ISS sites and IFA (indicated by dashed borders), showing locations and ranges of shipboard Doppler radars, with 5° square outlined in bold indicating AIP-3 study area.

SSM/I retrieval, the vertical divergence (convergence) of eddy fluxes of moisture (sensible heat) are obtained by residues based on Eqs. (1) and (2),

$$L_v\frac{\partial\overline{q'\omega'}}{\partial p} = Q_2 - [L_v(\overline{c} - \overline{e}) + \varepsilon] \quad \text{and} \qquad (13)$$

$$-\frac{\partial\overline{s'\omega'}}{\partial p} = Q_1 - [L_v(\overline{c} - \overline{e}) + \varepsilon] + Q_R, \qquad (14)$$

where ε is the vertically dependent calibration adjustment to the initially retrieved heating, with a characteristic value of ~6% of the heating rate and a worst-case value of ~20% for large rain rates. The covariances are contributions of unresolved eddies to Q_1 and Q_2, representing important quantities in understanding the role of cumulus convection on tropical energetics.

3. Datasets

The satellite data used in this study consist of a time series of SSM/I measurements extending over the TOGA COARE IOP. [Note that measurements from the Tropical Rainfall Measuring Mission (TRMM), launched in November of 1997 and carrying a spectrally enhanced SSM/I-type radiometer called the TRMM Microwave Imager plus a 14-GHz precipitation radar, are just now beginning to emerge as an important new piece of information on tropical rainfall; see Simpson et al. (1996) and Kummerow et al. (1998).] Before the rain retrieval process is applied, the brightness temperatures at 19 and 37 GHz are enhanced spatially to the ~13-km ground resolution of the 85-GHz channels to obtain spatial resolution consistency across the different channels. This consistency is important mainly for radiative transfer calculations that take place within the retrieval algorithm. A description of the energy-conserving spatial deconvolution scheme is found in Farrar and Smith (1992); a study of the scheme's impact on SSM/I precipitation retrieval has been described by Farrar et al. (1994).

The sounding data required for the large-scale diagnostic heat and moisture budgets were derived from Integrated Sounding System (ISS) measurements taken four times per day at each of the eight TOGA COARE ISS sites (Fig. 1). The general philosophy behind the ISS design, descriptions of the individual instruments, and the advantage of this kind of multisensor sounding system have been described by Parsons et al. (1994). Interpolated values at a constant pressure increment of 5 hPa provided by the National Center for Atmospheric Research were used in the analysis. Although there is uncertainty involved in the magnitude of moisture measurements, this issue was partially addressed in the data processing (Miller 1994). In addition, the expected degree of moisture uncertainty does not significantly effect the vertical structure of heat and moisture budgets (M. Yanai 1997, personal communication).

At the time of TOGA COARE, two satellite platforms (*F10* and *F11*) from the Defense Military Satellite Program were in orbit. Each platform provided two daily snapshots of all or part of the IFA domain. Thus, there were four daily observations around the times of 0700, 1100, 1900, and 2200 UTC, which corresponded well with the ISS sounding times of around 0500, 1100, 1700, and 2300 UTC. The overall daily coverage of IFA by the two sets of SSM/I measurements was better than 85%. Therefore, neglecting diurnal variability, the SSM/I measurements provided the basis for making adequately sampled daily rain-rate and latent heating retrievals.

Uncertainties with the TOGA COARE radar rain rates has been a long-term issue. The mean value of the first version of IFA radar rain rates was found to be significantly negatively biased, with the mean of the second version increasing by about 30%–50% (Short et al.

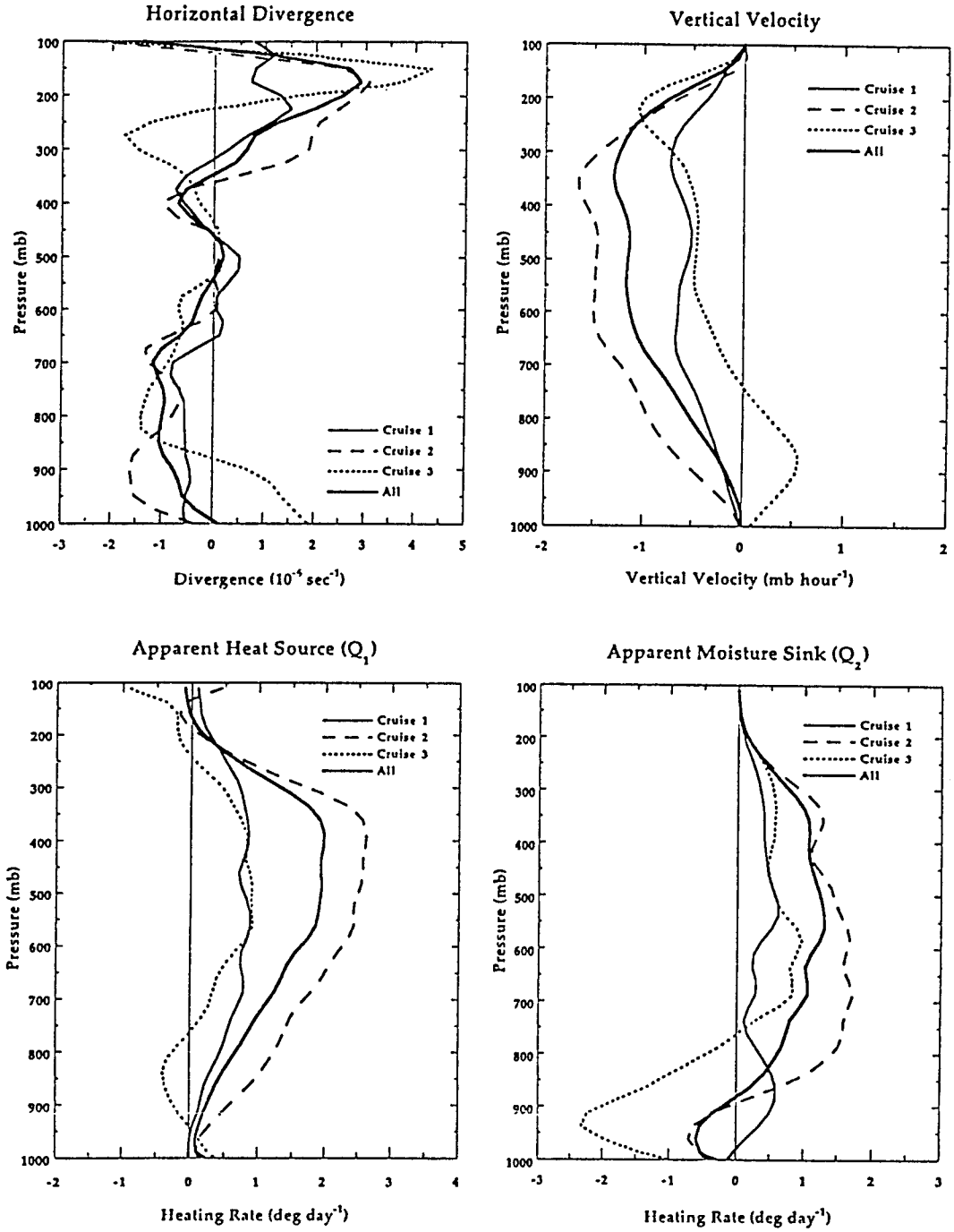

FIG. 2. Mean vertical profiles of horizontal divergence (top-left panel), vertical velocity (top-right panel), Q_1 (bottom-left panel), and Q_2 (bottom-right panel) for all three individual TOGA COARE cruises and all-cruise composite.

1997). Nevertheless, the mean of the second version still was found to be lower by ~30% (in conjunction with the median) and ~48% (in conjunction with the mean) relative to a composite result taken from a number of SSM/I satellite algorithms used in the third Algorithm Intercomparison Project (AIP-3); AIP-3 was conducted by the Global Precipitation Climatology Project over the TOGA COARE study area (Ebert 1996). By the same token, there was agreement between the radar and satellite for the retrieved rain patterns (Ebert and Manton 1998).

An independent surface precipitation dataset based on ship and ISS-site rain gauge measurements was used to obtain daily rainfall over IFA for comparison with

the SSM/I retrievals and for the moisture budget studies. In this analysis, any measured daily rainfall values were considered to be unreliable if measurements were missing around any of IFA's four corners.

Because most soundings reached 100 hPa, and this pressure level is near the tropopause in a tropical atmosphere, the 100-hPa level and the surface were chosen as the top and bottom boundaries for the Q_1 and Q_2 budget analysis. All missing data were first replaced using linear interpolation and then checked for vertical consistency by comparison with nearby soundings. After applying a 25-hPa running average over the high-resolution profiles, data points selected at the surface and upward in 25-hPa intervals were used for the final analysis. This procedure prevents aliasing by turbulence processes. Given the occurrence of missing data at the regular sounding times and to preserve the length of the IOP record, daily averages at each ISS site were assembled for the budget analysis. To avoid analysis inconsistencies, data were discarded if no measurements were reported at any of the four IFA corners. Upon completion of the quality-control and interpolation procedures, a 78-day time series of budget results was obtained.

4. Averaged kinematic and diabatic heating processes

a. Divergence, vertical velocity, and Q_1–Q_2 profiles

The averaged profiles of mean horizontal divergence, vertical velocity, and Q_1–Q_2 for different timescales over the TOGA COARE IFA, which help to underscore the general meteorological features, are shown in Fig. 2. The large-scale divergence and vertical velocity calculations have been mass adjusted so that ω is forced to zero at 100 hPa. There are three cruise periods based on the two IFA shipboard radar platforms. The periods are 1) 11 November 1992–10 December 1992, 2) 15 December 1992–18 January 1993, and 3) 23 January 1993–23 February 1993. Because of missing soundings, the reliable sample-day counts for the three cruise periods are 28, 31, and 19, respectively, for a total sample of 78 high-quality days.

Figure 2 depicts vertical profiles for cruises 1, 2, and 3 and an all-cruise composite. It can be seen that the profile structures for cruises 1 and 2 are fairly similar, with the cruise-2 magnitudes for Q_1 and Q_2 exceeding those of cruise 1 by a factor of about 2. The profile structures for cruise 3 are different because of the fact that more than 40% of its sample days were inactive, that is, cruise 3 was a more suppressed period in an overall sense. The 78-day all-cruise composite divergence profile indicates maximum convergence and divergence levels at 700 and 175 hPa, respectively, largely consistent with cruises 1 and 2. In comparison with the mean divergence profile over the summer western Pacific area, where, according to Yanai et al. (1973), the maximum convergence and divergence are at 950 and 200 hPa, there is some suggestion that the cloud systems over IFA are generally deeper and more dynamically complex at midlevels. Yanai et al. used 18% more days of data, however, which may have produced more smoothing. There is a broad range of relatively large upward motion from 250 to 700 hPa, with a maximum of 1.3 hPa h^{-1} at 350 hPa for the all-cruise composite. The profiles of mean ω over IFA and the summer western Pacific from Yanai et al. are similar; the magnitude is three times larger for the latter, however.

The 78-day, all-cruise composite Q_1 profile is consistent with results from Shaack et al. (1990) and Frank and Wang (1996), although the magnitudes of maximum heating are larger in these two studies because of different calculation schemes, averaging periods, and locations. Similar features are found in the Q_2 profiles. Overall, there is drying above 900 hPa, with a maximum of 1.3° day^{-1} near 550 hPa. Unlike the summer western Pacific, in which Q_2 indicates maximum drying near 800 hPa, Q_2 in IFA does not have a clear secondary maximum drying layer in the lower troposphere (a more detailed comparison with published studies is given in section 4c). This result may indicate that convection over the wintertime IFA is not as active as in summer.

A comparison of estimated and measured daily mean surface rain rates from SSM/I and shipboard/ISS-site rain gauges over the TOGA COARE IFA is shown in Fig. 3. Measured daily surface rainfall involves uncertainty stemming from objectively analyzing measurements whose spatial scale of variability is generally smaller than the distances between measuring sites. Also, the breaks in the time series indicate that there are deficiencies in the rain gauge measurements during these periods. The agreement between measurements and retrievals is strong, however. Although the 78-day-mean measured surface rainfall is larger than the retrieved value, most of that difference is the result of a large difference over a short period around 4 January (day 65). Otherwise, the daily variations and magnitudes of the estimated and measured rain rates are consistent. The difference on day 65 is from insufficient SSM/I sampling; that is, there was only one SSM/I swath passing through the IFA region on that day. The correlation coefficient is 0.68 at the 1% significance level. There are a number of days with little rain over IFA during IOP, indicative of prevalent nonconvective rain systems within the warm pool. The averaged measured daily mean rain rates over IFA, based on the reliable ISS days for cruises 1, 2, and 3, are 6.4, 16.8, and 6.1 mm day^{-1}. This result highlights that convection during cruise 2 was much more active than during cruises 1 and 3. Note that the cruise-to-cruise variations in rain-rate behavior are consistent with that for divergence, vertical velocity, and Q_1–Q_2.

b. Convective–stratiform heating–moistening structures

The averaged horizontal divergence, vertical velocity, and Q_1–Q_2 profiles discussed above statistically blend

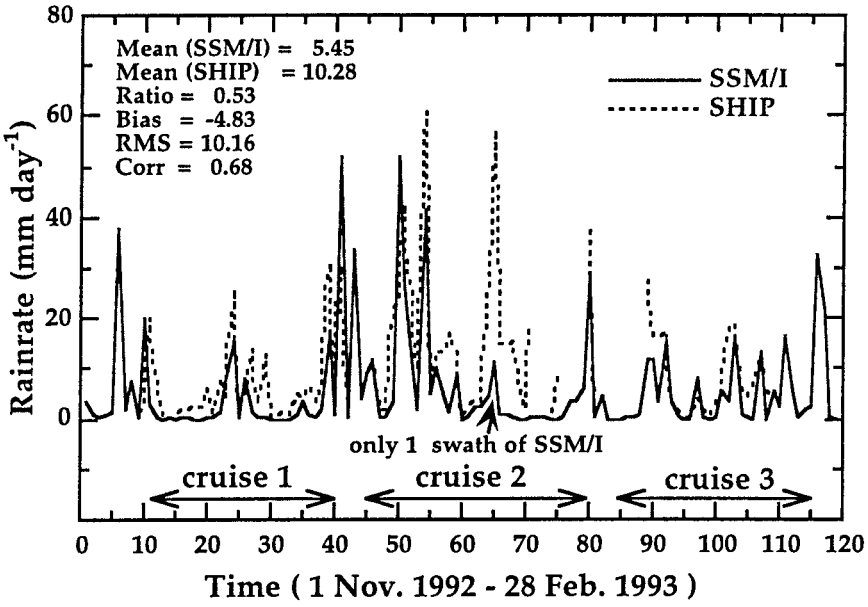

FIG. 3. Comparison of daily surface rain rates from SSM/I and shipboard–ISS-site rain gauges over IFA.

the dissimilar nature of the distinct convective and stratiform rain systems. Any classification of convective and stratiform systems over IFA that is based on daily datasets is not ideal because the two categories represent separate phases in precipitation life cycles, which generally occur over short time intervals (a few minutes to a few hours) and mesoscale-type spatial domains (10–100 km). Daily timescale- and IFA space scale–based classification is optimal for analyzing retrieved latent heating information from the SSM/I measurements, however, because this procedure addresses the minimum scales needed to obtain sufficient sampling for the retrievals themselves. We emphasize that further investigations involving near-instantaneous classification of convective and stratiform rain structures would enable better understanding of the detailed heating–moistening processes under the diverse tropical ω regimes.

It is known that the vertical structures of Q_1 and Q_2 for convective and stratiform conditions are very different (e.g., Johnson 1984). In general, upward vertical motion throughout part or all of the troposphere is associated with convective systems, and low-level downward tropospheric motion capped with upward motion above indicates the presence of stratiform rain (Houze 1989). Because the TOGA COARE radars saw only half of IFA, it is questionable whether the merged radar dataset is the best choice for making the convective–stratiform classification for the satellite-based analysis. Therefore, we have adopted the approach that, given the heterogeneous nature of the occurrence and distribution of convection cells and their evolution into stratiform rain and the close relationship between ω structure and rain phase, a classification system based on area-wide ω gives rise to the best results.

In so doing, 20 distinct convective and 6 distinct stratiform days were chosen from the 78 samples for independent compositing based on features in the ω profiles consistent with mostly convective or mostly stratiform. According to this approach, the mean rain rate from ship rain gauges is 19.2 mm day^{-1} for the convective case and 14.7 mm day^{-1} for the stratiform case. An independent check of the radar datasets also indicated more rain coverage and convective activity for the selected convective days. [Detailed information about the TOGA COARE radar-based rain datasets is given in Short et al. (1997).]

The composite horizontal divergence, vertical velocity, and Q_1–Q_2 vertical distributions (plus their standard deviations) are shown in Figs. 4a,b. It can be seen that, for convective situations (Fig. 4a), the horizontal divergence profile exhibits convergence below 375 hPa, with a maximum of -4.3 μs^{-1} around 850 hPa, and divergence above 375 hPa, with a maximum of 10.3 μs^{-1} near 200 hPa. The ω profile indicates upward motion throughout the troposphere, with a maximum of -5.9 hPa h^{-1} at 350 hPa. Positive heating appears throughout almost the entire troposphere, with a maximum of 9.5° day^{-1} near 425 hPa. The Q_2 profile shows drying throughout almost the entire troposphere, with a maximum of about 6.0° day^{-1} near 525 hPa. A second peak near 675 hPa is present but not as obvious.

For the stratiform case (Fig. 4b), convergence is found between 350 and 800 hPa and above 150 hPa, with a maximum at 650 hPa. Divergence is found below 800 hPa and between 150 and 350 hPa, with maxima near the surface and 200 hPa. There is sinking motion below 650 hPa and rising motion between 200 and 650 hPa. The maximum heat sink is below 650 hPa, with a

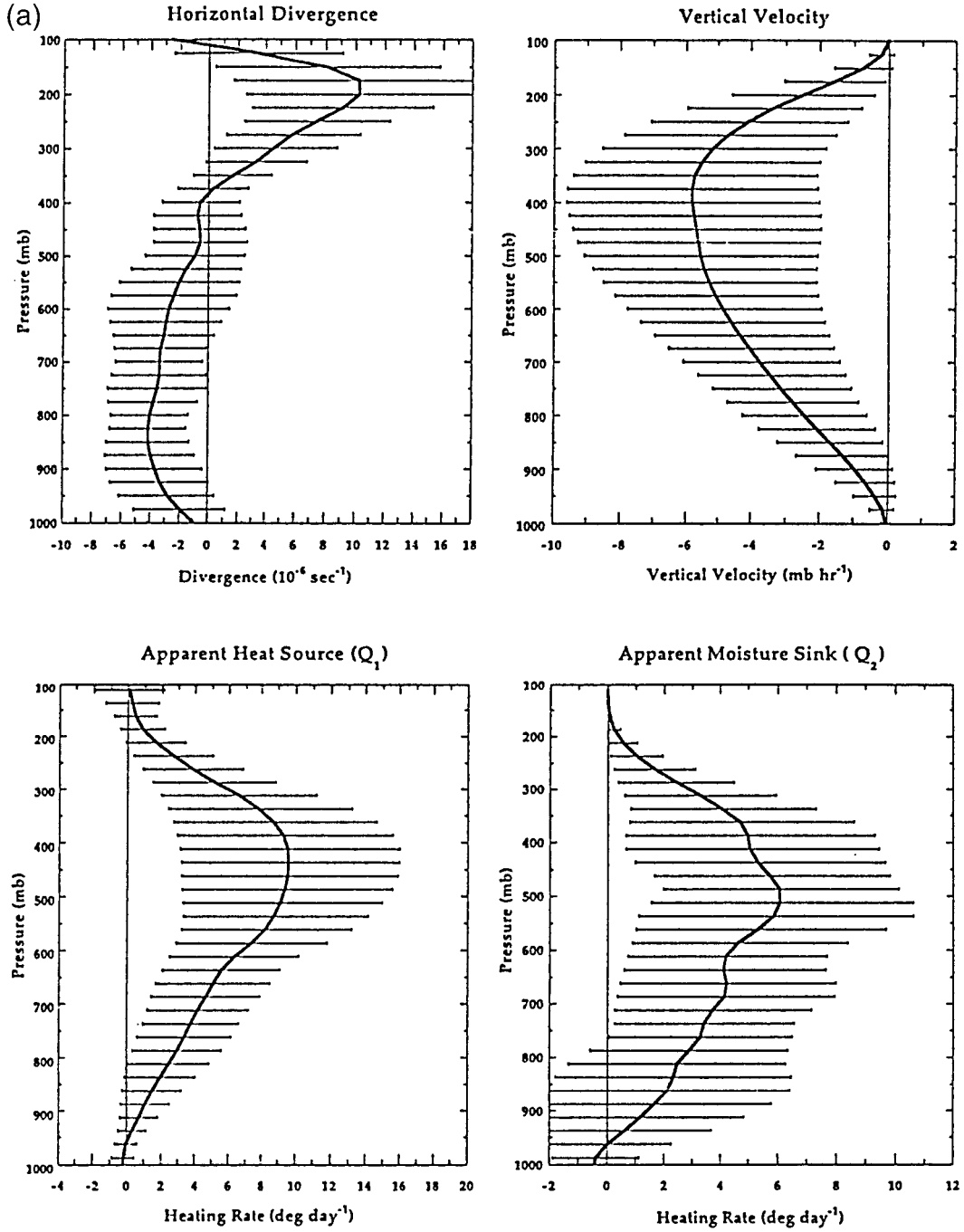

FIG. 4. Composite vertical structures of horizontal divergence, vertical velocity, Q_1, and Q_2 and associated standard deviations over IFA area for (a) convective systems and (b) stratiform systems.

secondary sink above 250 hPa. Maximum heating of 2.5° day^{-1} is found near 400 hPa, and the maximum heat sink of 1.1° day^{-1} is found at 750 hPa. The Q_2 profile shows peak drying of 1.5° day^{-1} near 450 hPa and peak moistening of $-4.0°$ day^{-1} near 750 hPa. The ranges in standard deviations suggest that the underlying vertical structure properties of the selected convective and stratiform realizations are consistent.

A comparison of the vertical structures of horizontal divergence, ω, and Q_1 for IFA convection to long-time mean properties of these quantities for the Northern Hemisphere summer western Pacific area (Yanai et al. 1973) indicates similarities in structures and magnitudes. The dominant Q_2 peak at 800 hPa in the summer western Pacific region is not apparent over the IFA winter region, however. There are two possible reasons for

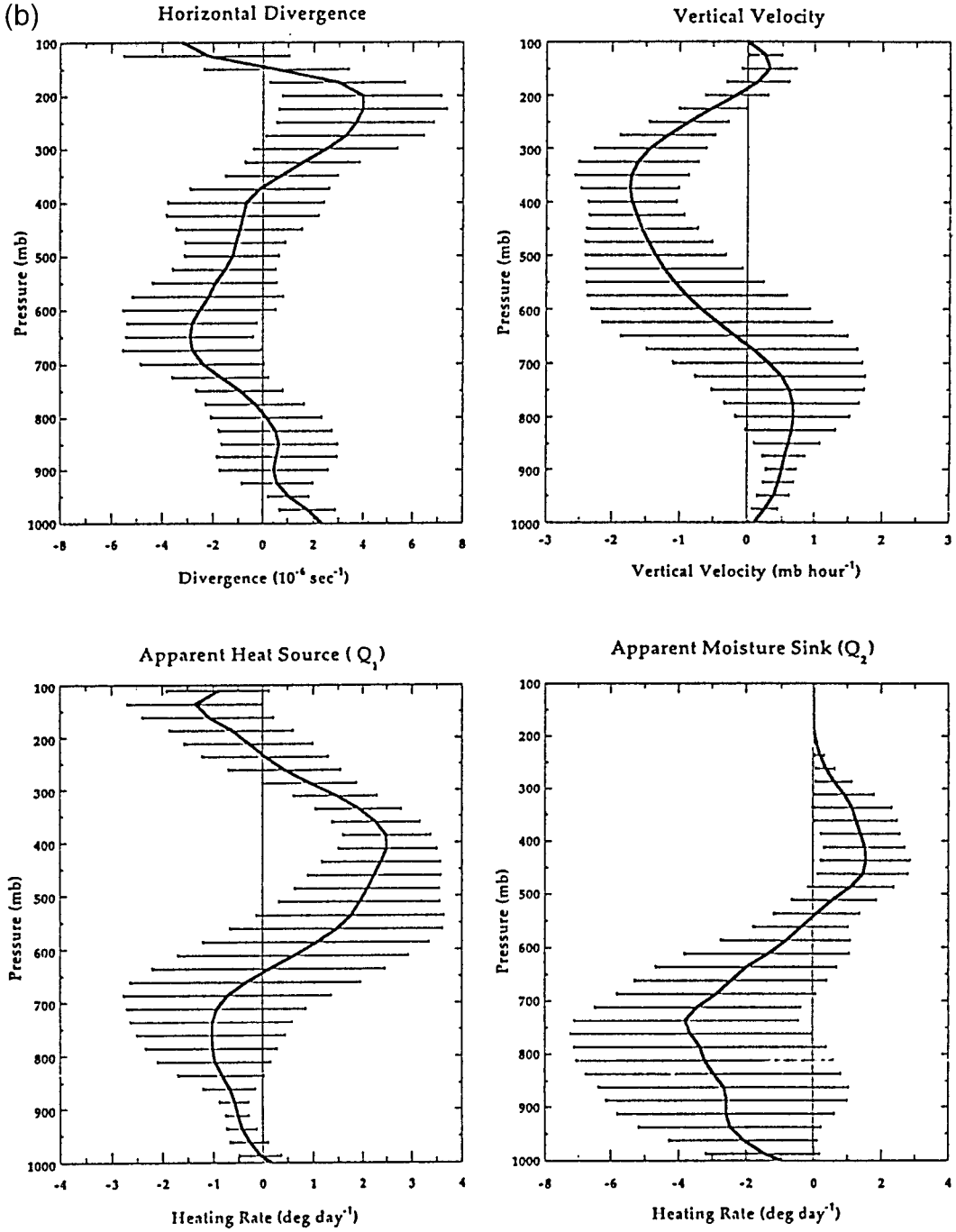

FIG. 4. (*Continued*)

this difference. First, because daily mean sounding data were used in this study, the convective cases selected here may be blurred by stratiform effects, which would reduce the underlying intensity of convective profiles. Alternatively, this difference may be a distinguishing Q_2 feature between summer and winter regimes. Results based on a limited but highest-quality four-sounding-per-day data period over IFA (Yang and Smith 1999a) indicate that the general profile structures of ω and Q_1 for convection are similar to the features described above, and Q_2 has a secondary peak near 775 hPa. This secondary peak is not the dominant drying process as with the NH summer western Pacific area, however. Because analyzing on the daily timescale is not likely to be the major reason for producing the Q_1–Q_2 differences, we presume that winter conditions are primarily

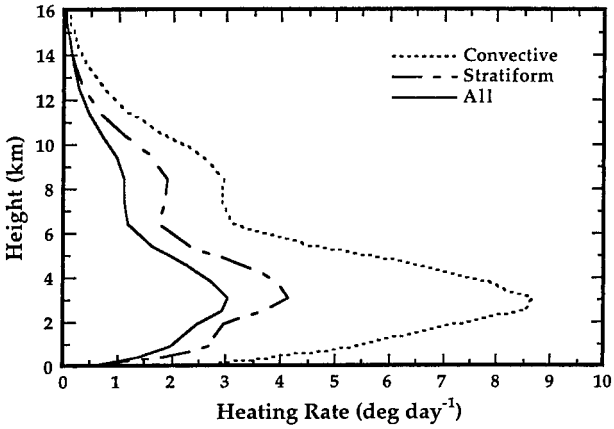

FIG. 5. Vertical structures of averaged latent heating derived from SSM/I measurements for convective, stratiform, and 78-day composites over IFA.

responsible for producing profile structure differences in the vertically resolved apparent moisture sink. These results suggest that stratiform activity is more pronounced in the tropical boreal winter.

The averaged vertical distributions of latent heating derived from SSM/I for convective, stratiform, and the all-day cases are shown in Fig. 5. It is seen that large heating magnitudes are located between 1 and 10 km, with a peak near 3 km. Latent heating is much stronger for convection than for stratiform precipitation, with maxima of 8.3° and 4.2° day^{-1}, respectively. Overall, maximum latent heating is about 2.9° day^{-1}. The similarity in vertical structures, especially in the lower troposphere, implies that the retrieval algorithm contains deficiencies in resolving the two distinct types of precipitating cloud systems. In general, the latent heating structure for stratiform precipitation in the lower troposphere seems unrealistic. Because grid-averaged cloud model–generated hydrometeor profiles were used as the supporting microphysical database for the retrieval algorithm, that is, from the Tripoli (1992) University of Wisconsin nonhydrostatic mesoscale model, it would appear that the chosen grid scale is not properly distinguishing some key differences between convective and stratiform rain. In other words, the convective–stratiform features are being blended in the grid averaging at the stage of preparing the retrieval algorithm's cloud microphysical database.

Nevertheless, latent heating profiles associated with convective and stratiform clouds can be discriminated based on the magnitude of midtropospheric heating. Thus the results of Fig. 5 provide some quantitative measure of the main difference in diabatic heating between active and decaying convection. In any event, increasing the grid resolution of the inner nests of cloud models used to support physically based PMW rain retrieval algorithms should provide better initial-guess microphysical behavior for precipitation inversion algorithms. This improvement would, in turn, lead to better characterization of the retrieved latent heating profiles.

c. Comparison with previous results

It is instructive to compare the Q_1–Q_2 profiles for the TOGA COARE IFA with profiles found by other investigators for oceanic regions. Cloud systems examined in previous studies have been located in a number of different areas, with the associated rain-rate intensities and time records varying from place to place. Thus, the comparison is more meaningful if rain-rate normalization is applied. Figure 6a illustrates the mean Q_1 profiles from different studies normalized to a daily rain rate of 1 cm day^{-1}. Current (mean) represents the mean Q_1 profile over the 78 TOGA COARE study days, and current (combined) represents the mean Q_1 profile over the 26 selected days used for the convective and stratiform composites. The profiles for the summer western Pacific, Australian Monsoon Experiment (AMEX), IFA, and current (combined) represent one mode, exhibiting large magnitudes, with a maximum near 400–500 hPa. The current (combined) and Lin and Johnson (1996) results exhibit good agreement. The profiles for the SPCZ and current (mean) exhibit smaller magnitudes, with a maximum near 400–500 hPa.

Because the Yanai et al. (1973) Q_1 profile is averaged over a relatively long time for the summer western Pacific, their results provide the best comparison with this study's averaged results (i.e., TOGA COARE). It can be seen that the mean magnitude of Q_1 in IFA (current mean) is smaller than in the summer western Pacific, and the current (combined) value is similar to the Yanai et al. result. This result indicates that convective activity is not as prevalent in IFA as in the summer western Pacific equatorial region. The difference of Q_1 magnitudes between current (mean) and Frank and Wang (1996) may be caused by the fact that this study averaged Q_1 over only the 78-day reliable IFA sounding data period, and Frank and Wang applied their interpolated IFA dataset to replace the missing IFA sounding measurements for many days to obtain a 120-day time series of Q_1. Note that the current (mean) profile is very close to that for the SPCZ, especially Miller and Vincent's (1987) result. This similarity can be explained by the fact that both of them are based on measurements in the winter central Pacific equatorial area. In addition, the current (mean) profile is similar to the winter averaged heating profile over the SPCZ from the 15-yr National Centers for Environmental Prediction reanalysis dataset (Yanai and Tomita 1998).

Therefore, there are three independent results that indicate convection is more active in summer than in the winter over the tropical Pacific, although this agreement does not provide conclusive final evidence. Two alternative explanations should be considered. The first is that there are many inactive days in the selected IFA datasets that might be statistically nonrepresentative.

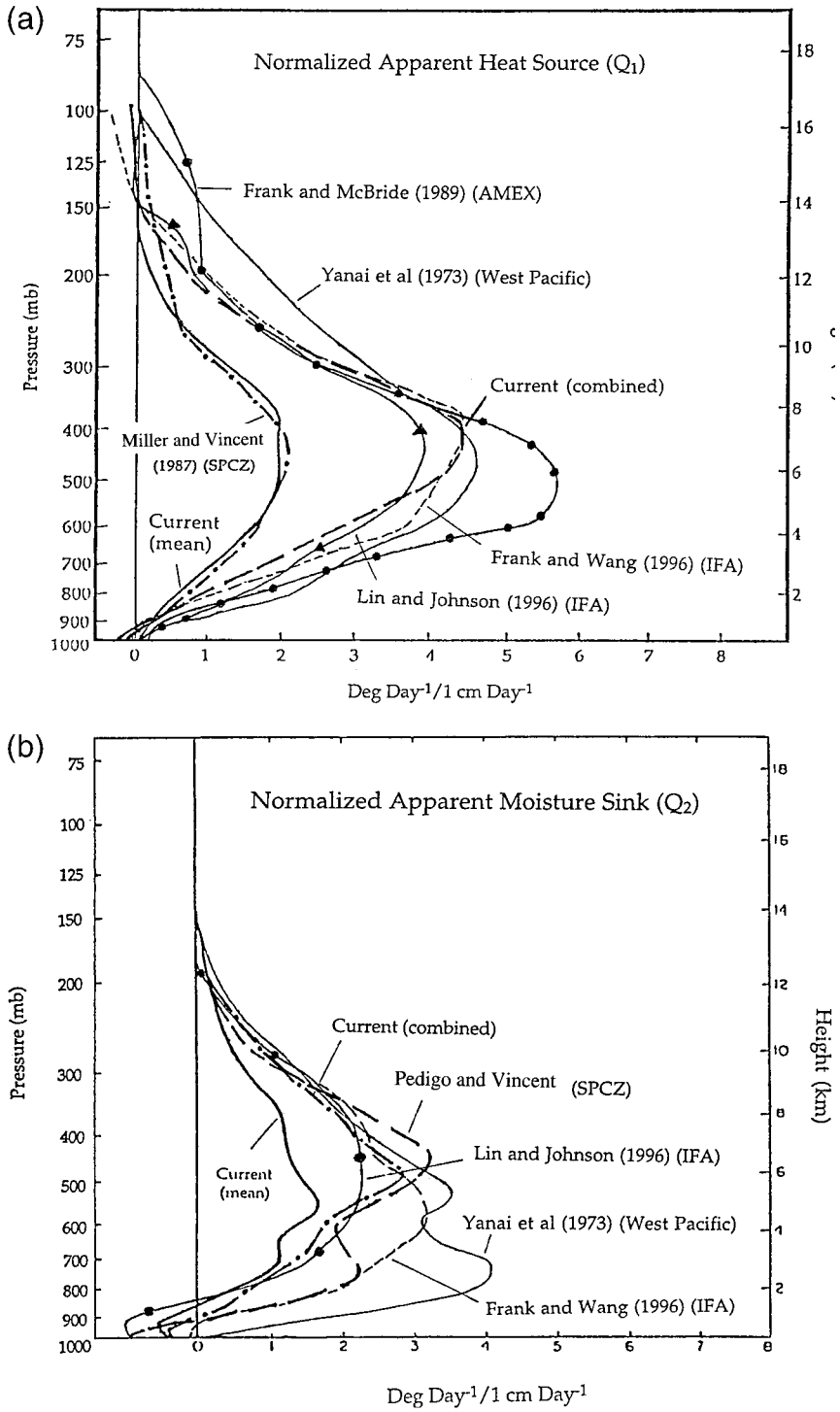

FIG. 6. Comparison of mean rain-rate-normalized (a) Q_1 profile and (b) Q_2 profile over IFA with those of previously published studies.

The second is that there was an eastward shift of the SPCZ caused by the 1992/93 El Niño event that may have led to some of the convective activity migrating out of IFA (Bell and Basist 1994; Rasmusson and Carpenter 1982). Further studies using TRMM datasets are expected to provide more exact understanding.

A comparison of rain-rate-normalized Q_2 profiles is given in Fig. 6b. All profiles exhibit two dominant

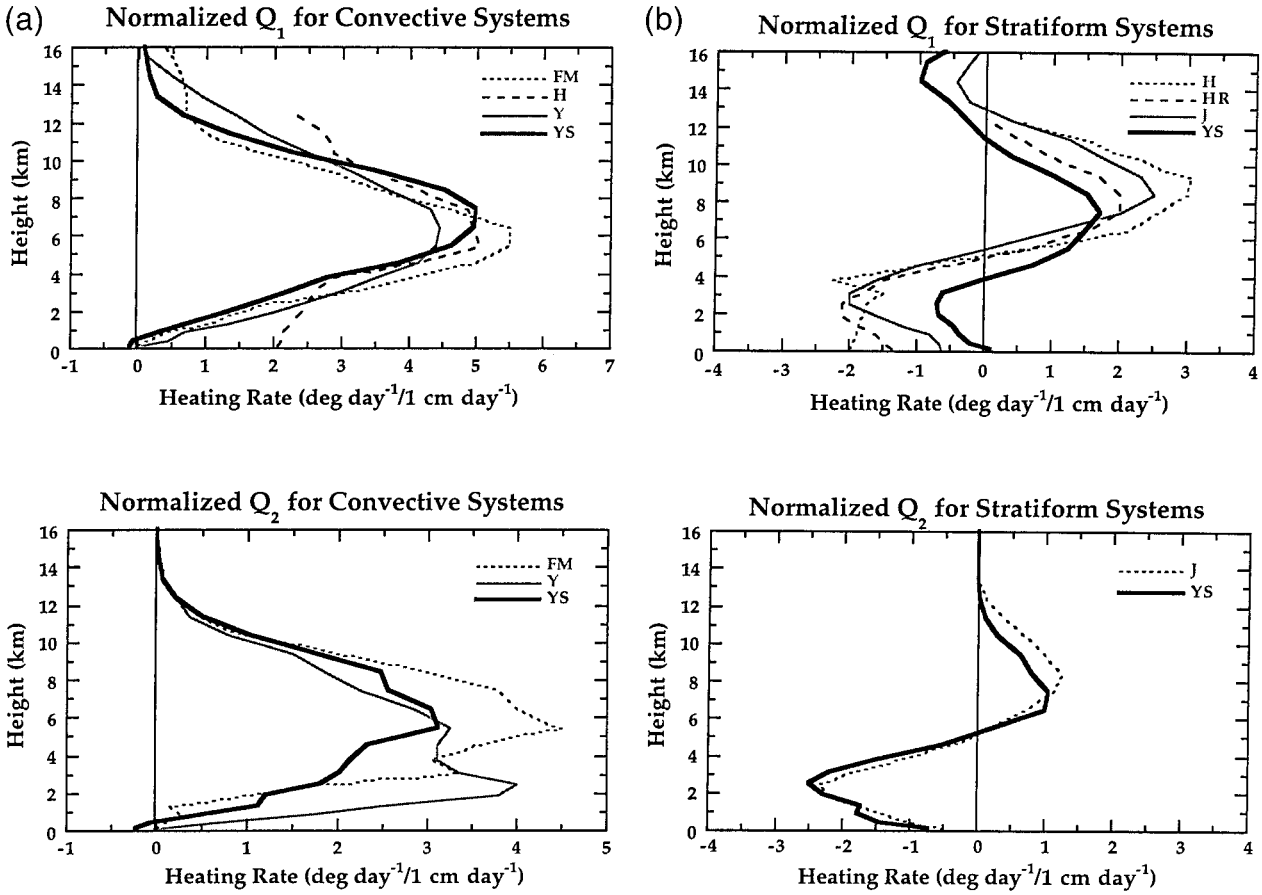

FIG. 7. Comparison of rain-rate-normalized Q_1 (top panel) and Q_2 (bottom panel) profiles for (a) convective systems and (b) stratiform systems.

peaks, which are the combined result of drying from both convective and stratiform processes. Both peaks are found in the lower troposphere. The shapes and magnitudes of the Q_2 profiles from current (combined) and Lin and Johnson (1996) are similar. The magnitude of the Q_2 profile from the Frank and Wang (1996) 120-day-mean result is larger than the current (mean), however. It also is larger than the Lin and Johnson convective case. The reason for this difference was discussed in the above Q_1 comparison. Over the SPCZ (Pedigo and Vincent 1990), the upper peak is the level of greatest drying, as is the case over IFA. The low-level peaks for both current (mean) and current (combined) are weak. This result further suggests that convection in IFA during winter is not as prevalent as in the summer.

The comparisons of rain-rate-normalized Q_1 and Q_2 profiles for convection are shown in Fig. 7a. Curve H is from Houze's (1982) Global Atmospheric Research Programme Atlantic Tropical Experiment (GATE) analysis. Profile Y is the averaged result for the summer western Pacific area (Yanai et al. 1973). Profile FM is from the study of convection for AMEX (Frank and McBride 1989). The bold line (YS) is the 20-day convective regime average for IFA from this study. The Q_1 profiles for convection are similar, with a maximum heating rate located at 5–8 km (top panel). The slightly smaller magnitudes of Q_1 from the Yanai et al. study might be caused by the longer averaging period. The Q_1 profiles are also consistent with the averaged heating profile of convective periods over IFA (Lin and Johnson 1996). Similar results are found in the Q_2 profiles (Fig. 7a, bottom panel). The vertical structures for IFA and AMEX are similar. The slight moistening near the surface (negative heating rates) for the IFA result possibly is due to surface evaporation driven by strong winds during the convection life cycle, coupled to vertical eddy moisture flux driven by turbulent processes. The Q_2 profile (YS) is also consistent with the mean result from Lin and Johnson (1996).

Figure 7b shows the comparisons of rain-rate-normalized Q_1 and Q_2 profiles for stratiform conditions. The notation used for these profiles is the same as for Fig. 7a, except now curve J is included from the Johnson (1984) study of Winter Monsoon Experiment (MONEX), as is curve HR from the Houze and Rappaport (1984) eastern Atlantic study (for Q_1 only). The Q_2 profiles for IFA and Winter MONEX are very similar at all levels, whereas the four Q_1 profiles are similar in

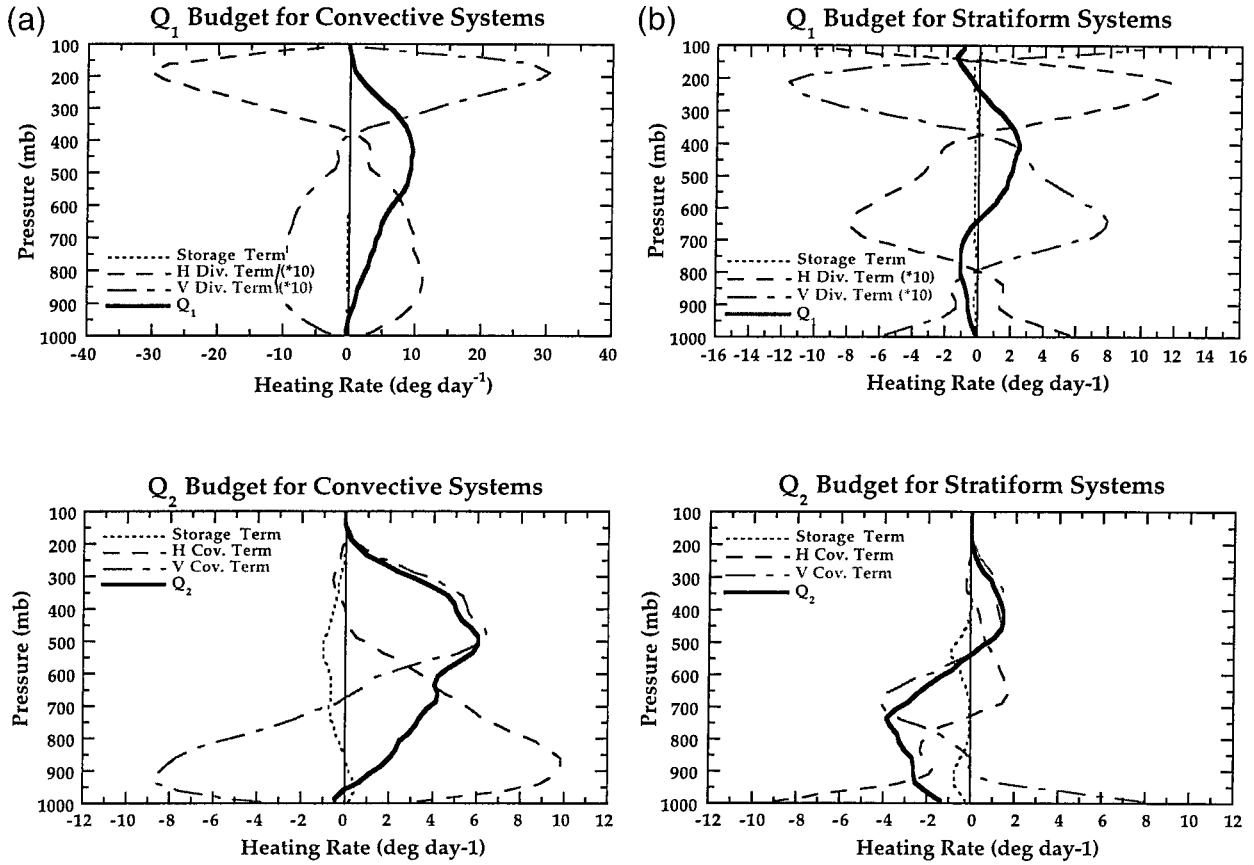

FIG. 8. Vertical profiles of Q_1 (top panel) and Q_2 (bottom panel) budgets for (a) convective systems and (b) stratiform systems over IFA.

structure but varying in amplitude at the peak heating and cooling levels. The only detectable difference in the two Q_2 profiles is that the level of maximum drying for IFA is slightly lower. This slight difference could be caused by the use of daily mean sounding data, because this type of daily averaging procedure can result in contamination by periods of weak convection.

The intercomparison results suggest that, in general, heat and moisture vertical structures for convective and stratiform situations are similar over different areas, with their magnitudes depending on the vertical development of embedded cloud systems. The results for convective heating profiles are different from the Houze (1989) results because different samples were used for the analysis. The convective vertical heating structure is dependent mainly on the associated vertical motion field so that similar ω profiles generally lead to similar heating structures.

5. Q_1–Q_2 budgets

a. Vertical distributions for convective and stratiform cases

The purpose of this section is to explore the mechanisms of heat and moisture budgets for convective and stratiform conditions over the TOGA COARE IFA. From Eqs. (1), (2), Q_1 and Q_2 are composed of storage and horizontal–vertical divergence terms. The minus sign should be noted in the Q_2 budget. Figure 8a shows the averaged vertical distributions of the Q_1–Q_2 budgets for convection. For Q_1 (top panel), the storage of dry static energy is almost negligible. The horizontal divergence and vertical divergence of dry static energy flux are the two dominant terms, with opposite sign. Although Q_1 mainly depends on the difference between two large terms, as discussed in Yang and Smith (1999a), the diagnostic scheme used for these calculations has been shown to be reliable. Horizontal divergence contributes to positive heating below 350 hPa and to negative heating (cooling) above. The vertical divergence is negative below 350 hPa and positive above. Overall, Q_1 is positive throughout the troposphere with a maximum near 450 hPa. That is to say, horizontal divergence plays a more important role in the middle–lower troposphere, and vertical divergence plays a more important role in the upper troposphere.

Physical processes that influence the Q_2 budget for the convective case are different from those of the Q_1 budget (Fig. 8a, bottom panel). The loss of moisture from condensation is compensated for by large-scale

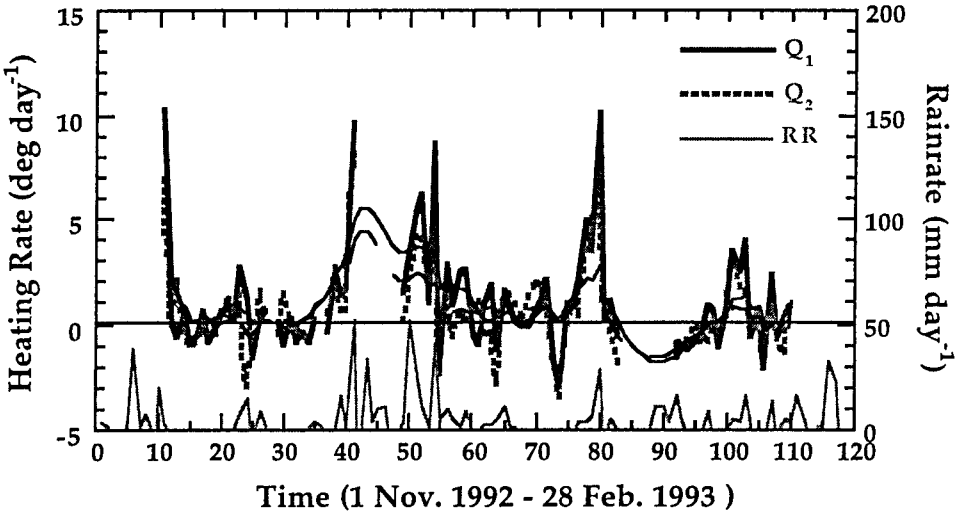

FIG. 9. Time series of vertically integrated, daily rain-rate-averaged Q_1 and Q_2 over IFA. Surface rain rates from SSM/I are shown at bottom of diagram. Thin solid and dashed lines are smoothed results of Q_1 and Q_2, respectively.

horizontal moisture convergence in the lower troposphere. Vertical moisture flux then transports the moisture surplus from the lower troposphere into the upper troposphere for balance.

A term-by-term analysis also is presented for the stratiform case. It can be seen from Fig. 8b (top panel) that the storage term of Q_1 still is small. The vertical distributions of horizontal and vertical divergence of dry static energy flux become more complicated, however. Overall, the heat sink below 650 hPa stems from two sources, that is, the vertical divergence term below 800 hPa and the horizontal divergence term between 650 and 800 hPa. The heat sink between 150 and 250 hPa and above 150 hPa comes from vertical and horizontal divergences of dry static energy flux, respectively. The heat source between 250 and 650 hPa is composed of contributions from the horizontal divergence term in the 250–350-hPa layer and the vertical divergence term in the 350–650-hPa layer. A similar situation also is seen in the Q_2 budget (Fig. 8b, bottom panel). The moistening processes below 500 hPa are mainly the result of vertical convergence in the 500–750-hPa layer and horizontal convergence below 750 hPa. The drying processes above 500 hPa mainly arise from vertical convergence of moisture flux.

In comparing the Q_1–Q_2 budgets for convective and stratiform conditions, it is evident that, in addition to the different vertical structures for various terms, the main difference is that the dominant term may change. For example, in the Q_1 budget, the dominant term for convection is not the dominant one for stratiform precipitation. For the Q_2 budget, however, differences in the most important term (in a relative sense), appear only in the 600–750-hPa layer. That is, the dominant term between 600 and 750 hPa for convective conditions is horizontal convergence and for stratiform conditions is vertical convergence.

b. Temporal variations of mean tropospheric budget terms

To express the temporal characteristics of the diagnostic budgets, the vertically distributed latent heating retrieved from SSM/I and the Q_1–Q_2 profiles were first vertically integrated from surface to tropopause, then converted to mean tropospheric heating rates. Figure 9 shows the time series of daily surface rain rate and Q_1–Q_2 heating rates over IFA. It is evident that Q_1 and Q_2 have similar temporal variations, with fairly similar magnitudes. That is, the heat source corresponds primarily to drying, and the heat sink is the counterpoised moistening process. Based on Eqs. (3) and (4), this result indicates that total heating is due mostly to latent heating. Along with the daily timescale variations of Q_1 and Q_2, there are dominant heating and moistening peaks on days 11, 40, 54, and 80. These peaks suggest an underlying 20–30 day low-frequency oscillation. The smoothed Q_1 and Q_2 series in Fig. 9 provide an even clearer representation of this oscillation. The temporal variations are consistent with those from the Lin and Johnson (1996) study. The Gutzler et al. (1994) study on outgoing longwave radiation also indicated an intraseasonal oscillation during the TOGA COARE IOP. When compared with daily rain rates, the active period of the low-frequency oscillation always corresponds to large rain rates. The active period during days 40–53 is the most dominant for frequent convective activity; also see McBride et al. (1995).

The relationship between the atmospheric heat source and latent heating is shown quantitatively in Fig. 10a.

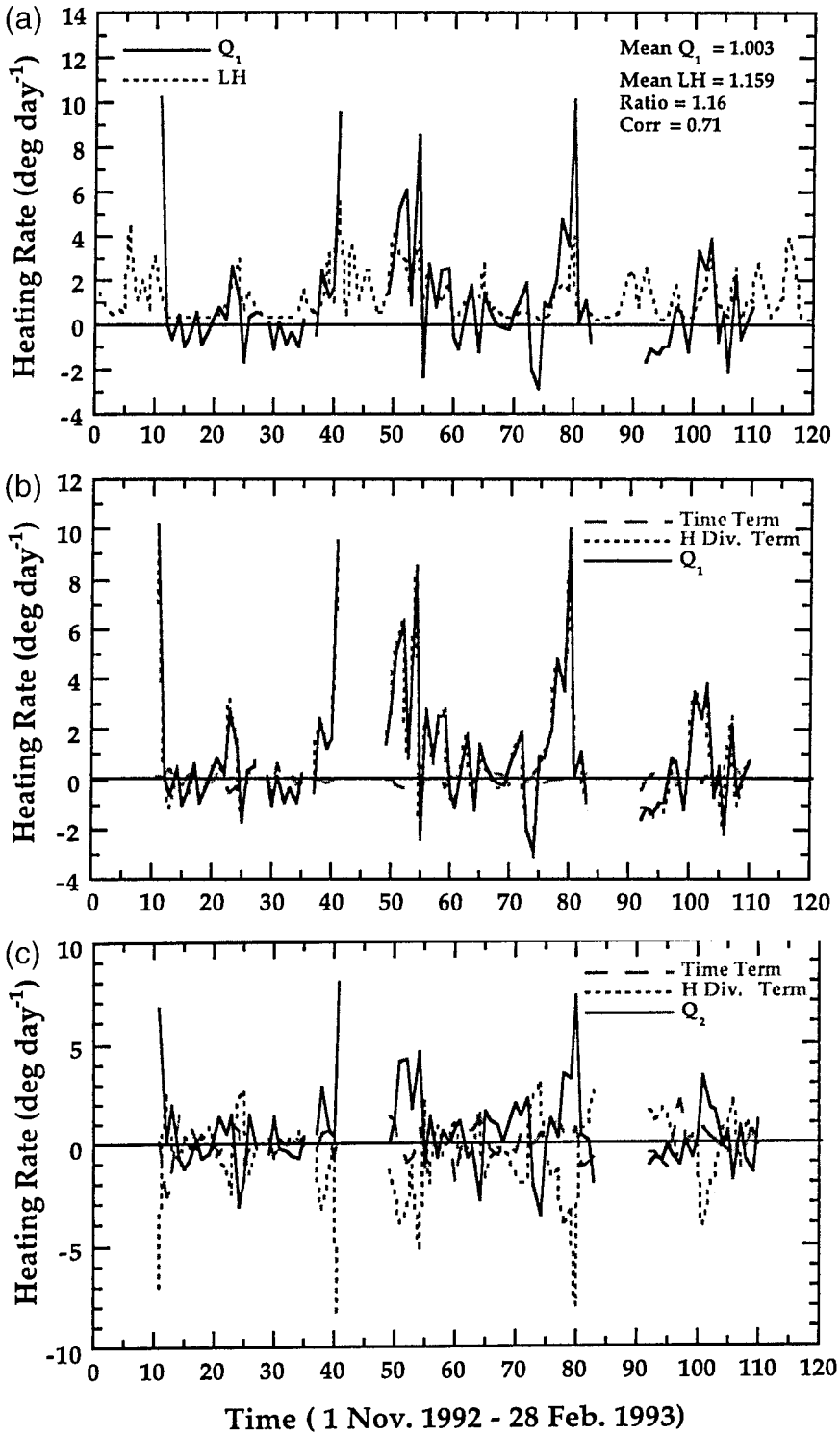

FIG. 10. Time series of vertically integrated, daily averaged (a) latent heating and Q_1, (b) Q_1 budget, and (c) Q_2 budget over IFA.

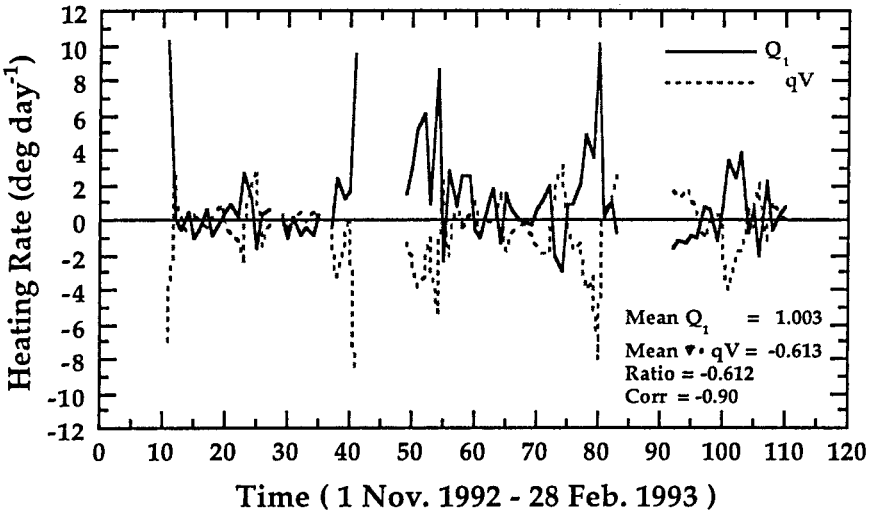

FIG. 11. Comparison of vertically integrated, daily averaged heat source (Q_1) and horizontal divergence of moisture flux ($\nabla \cdot q\mathbf{V}$) over IFA.

Wherever there is a positive heat source, there also is related latent heating. Their correlation coefficient is 0.71 at the 1% significance level. The overall averaged latent heating is even larger than the mean Q_1. This result is caused by the averaging itself, which includes heat sinks because of the complicated physical processes embedded in Q_1. Actually, the latent heating contributes approximately 70% to the heat source if the averaging scheme is only applied to days of positive Q_1.

From the left-hand side of Eqs. (1) and (2), the vertical divergence terms (associated with mean vertical motion) of dry static energy flux and moisture flux adjust only the vertical distribution of heat and moisture. Their effects disappear after vertical integration of the governing equations. Figure 10b shows mean tropospheric heating rates from the Q_1 budget. It can be seen that the contribution from the storage term is small, and the horizontal divergence of dry static energy flux is very close to Q_1. Similarly, the Q_2 budget after vertical integration is shown in Fig. 10c; note that there is a minus sign associated with Q_2 (see Eq. 2). The magnitude of the storage term in the moisture budget is much larger than in the heat budget. There still is a major contribution to Q_2 from the horizontal divergence of moisture flux, however. Moreover, there is a strong relationship between storage and horizontal divergence. Their correlation coefficient is about -0.39 at the 1% significance level. This kind of relationship is not found in the AMEX dataset (McBride and Holland 1989). Figure 11 demonstrates the relationship between total heat source (Q_1) and horizontal divergence of moisture flux ($\nabla \cdot q\mathbf{V}$). The almost out-of-phase behavior is evident. Their correlation coefficient is -0.90, and their ratio is about -0.61. That is, some 61% of total heating comes from large-scale horizontal convergence of moisture flux.

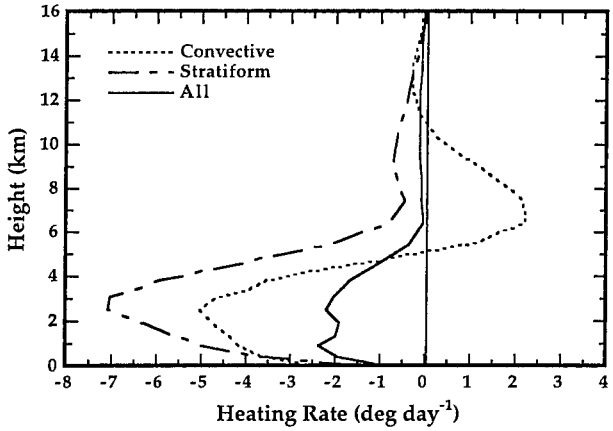

FIG. 12. Composite mean vertical divergence profiles of vertical eddy moisture flux for convective, stratiform, and combined conditions over IFA.

c. Estimates of eddy heat and moisture fluxes

After the latent heating and Q_1–Q_2 profiles are obtained, the vertical divergence of vertical eddy moisture flux can be estimated from Eq. (13), and the vertical convergence of vertical eddy sensible heat flux can be estimated from Eq. (14), given the appropriate radiative heating. Because uncertainties are involved in both the latent heat retrieval and Q_2 calculations, one must be cautious with estimates of the daily vertical divergence profiles of vertical eddy moisture flux derived from the residuals. To reduce uncertainty, a compositing approach is used, that is, the averaged vertical divergence profiles of vertical eddy moisture flux for convective and stratiform days are taken separately and then for all days combined (Fig. 12). It is evident that the magnitude of vertical divergence of vertical eddy moisture flux is similar to the magnitude of Q_2, indicating that cumulus-

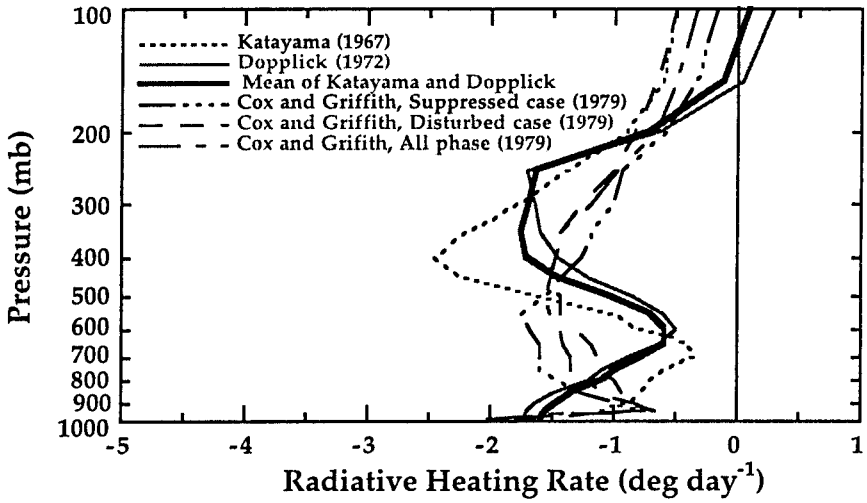

FIG. 13. Total radiative heating profiles (Q_R) from previously published studies.

scale processes are important in the moisture budget. For convective situations, eddy moisture flux dries the middle troposphere while moistening the lower and upper troposphere. Comparison with the Tao et al. (1993) model results indicates differences in the mid–lower troposphere, for which they showed drying near the surface and moistening in the midtroposphere. For stratiform situations, eddy moisture flux moistens the entire troposphere (with largest magnitudes in the lower troposphere). This kind of profile is different from the Tao et al. result, although their maximum moistening is located at a similar height. The averaged vertical divergence profile of vertical eddy moisture flux over all days shows moistening throughout the troposphere, with a peak near the 2-km level. The differences in the vertical divergence profiles of vertical eddy moisture flux may be caused by the fact that Tao et al.'s results were based on convective and stratiform regions in a squall line and these results were averaged over a large area containing mixed cloud systems. Note also that there is no additional independent source of measured eddy flux profile information to verify the retrieval results. Comparison with the results of Yang and Smith (1999a), based on the 17-day highest-quality IFA dataset, indicates that the multiday-averaged profiles are consistent. In general, the vertical divergence profiles of vertical eddy moisture flux for convective activity exhibit similar structure except in the lower troposphere, where moistening is found. For stratiform activity, however, the profiles are different, although the magnitude of maximum moistening is found at a similar height. These differences may be caused by the different sample sizes in the composites.

To calculate the vertical eddy flux of sensible heat, the radiative heating profile is required. Because radiative heating profiles are not available yet from the TOGA COARE data archive (only bulk tropospheric radiative heating estimates have been produced), averaged radiative heating profiles from other studies have been used. Katayama (1967) investigated the radiation budget of the troposphere over the Northern Hemisphere, generating monthly averaged total radiative heating profiles at different latitudes, including the Tropics. Climatological vertical profiles of Q_R also were generated by Dopplick (1972). Cox and Griffith (1979) investigated this quantity during Phase III of GATE. The radiative energy budget for the 1979 southwest summer monsoon was obtained by Ackerman and Cox (1987). Figure 13 shows various Q_R profiles from the above studies. The Katayama profile is the averaged profile between 150 and 160°E at the equator for January (from his Fig. 6a). The Dopplick profile is averaged between 0° and 5°S for December–February (from his Fig. 21). Cox and Griffith's results for different situations are also included. It is apparent that the Q_R profiles for the east Atlantic and west Pacific areas are different. Ackerman and Cox's Q_R profiles for the monsoon region (not shown) exhibit their own distinct characteristics.

Here, a characteristic profile of Q_R for IFA is based on a weighted average of the Katayama and Dopplick results, shown by the bold solid line in Fig. 13. The vertically integrated value is about -1.10°C day^{-1}. This value is higher than the -0.44°C day^{-1} value from radiation measurements made over IFA. Frank and Wang (1996) indicated that the TOGA COARE measured value is too low, however. They estimated a mean radiative cooling rate of -0.81°C day^{-1} over IFA, with magnitudes varying from -0.65° to -1.29°C day^{-1} for different array positions within IFA. Also, the estimated radiative cooling rate would be about -0.88°C day^{-1} over IFA if values of surface sensible and latent heat fluxes from Frank and Wang (1996) are applied to our reported Q_1 and Q_2 results. Therefore, the mean magnitude of the selected climatological radiative heating profile is in reasonable agreement with the estimated value used for the Q_1 budget calculations.

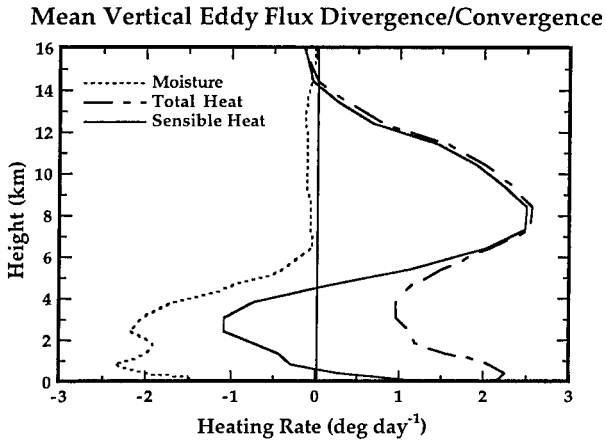

FIG. 14. Heating rates associated with mean eddy transport profiles of moisture, sensible heat, and total heat over IFA during IOP.

Figure 14 shows the mean vertical convergence of vertical eddy sensible heat flux and total heat flux, along with the vertical divergence of vertical eddy moisture flux for all days over IFA. The large magnitudes show that cumulus-scale processes are important in the heat budget and in the moisture budget. The dominant positive vertical convergence of vertical eddy sensible heat flux is found in the 5–10-km layer, with a maximum near 8 km. A small positive value is found near the surface. Negative vertical convergence of vertical eddy sensible heat flux is located between 1 and 5 km, with a maximum near 3 km. Note that the uncertainty generated by taking a climatological rendition of the radiative heating profile will have little effect on the vertical structure of the sensible heat flux convergence, as suggested above. The vertical convergence profiles of vertical eddy sensible heat flux are different from Tao et al.'s (1993) model results, which were of small magnitude and noisy throughout the troposphere. The vertical convergence of vertical eddy total heat flux is positive from the surface up to 14 km, with a very small negative value at the top of the troposphere. Its main peak is near 8 km, with a secondary peak near the surface. The location of maximum heating from the effects of cumulus-scale processes is similar to other results (e.g., Yanai et al. 1973; Esbensen and Wang 1988; Gallus and Johnson 1991).

As discussed in section 2, the vertical integral of vertical eddy moisture flux divergence is equivalent to surface evaporation. Thus, the reliability of the residual method for estimating vertical divergence of vertical eddy moisture flux can be assessed. The measured surface evaporation is obtained by applying the bulk aerodynamic method (see section 2), using ship-based sea surface temperature (SST) measurements made inside the IFA array. The comparison of estimated and measured daily mean surface evaporation over IFA is shown in Fig. 15. Statistics are given in the upper-left and bottom-right corners of the diagram. The pattern and magnitudes of the measured surface evaporation are generally consistent with the results of Lin and Johnson (1996), obtained by averaging measurements from four TOGA COARE buoys, although their time mean is 37% higher. This discrepancy might be caused by the fact that they averaged at the four buoy sites, but our results are averaged from 11 ship, buoy, and island sites.

Although the estimated surface evaporation is noisy on a daily basis, with a fairly large rms of ~6.0 mm day^{-1} and poor correlation (~0.15) relative to the measured values, the bias is only ~0.1 mm day^{-1}. Note also that, at times, the daily estimates exhibit nonphysical values below zero, stemming from taking differences between two large terms that each contain uncertainty. The temporal trends of estimated evaporation are consistent with the measured trends, however. This behavior is clarified when a weekly (7-day) running average is applied to the measured and estimated time series. The bold solid and dashed lines in Fig. 15 represent the smoothed results. Their correlation coefficient is ~0.5 at the 1% significance level, exhibiting a small bias (~0.03 mm day^{-1}) and a relatively small rms difference (~1.9 mm day^{-1}). These results suggest that, although the estimated vertical divergence of eddy moisture flux contains significant precision uncertainties on a daily basis, the systematic bias is small, and thus the noise can be reduced by time averaging or low-pass filtering.

Additional procedures were conducted to assess errors on estimated eddy flux divergence/convergence profiles. The first step was to study the effect of selections of daily convective Q_1 and Q_2 samples on their vertical structures. The Q_1–Q_2 profiles are the key elements in estimating the vertical divergence (convergence) profile of eddy moisture (sensible heat) flux. For one sensitivity test, six strong daily convective Q_1–Q_2 realizations were used in composite form to represent average heating–moistening conditions for convection. These magnitudes of Q_1 and Q_2 were about twice those from the originally selected 20-day composites. However, the rain-rate normalized vertical structures and magnitudes are similar for the two cases. This similarity suggests that the sampling selection of daily Q_1–Q_2 terms for the above analyses does not distort the representative vertical structures. Therefore, the sampling procedure should not affect significantly the vertical structure of estimated eddy flux convergence/divergence. Note, it also has been demonstrated that different methods for calculating Q_1 and Q_2 produce negligible differences (Yang and Smith 1999a). Last, although the errors in the sounding measurements will affect the accuracy of Q_1–Q_2, particularly errors in moisture and wind, these effects should not lead to more than 10% errors in magnitudes of Q_1–Q_2 based on the intercomparison analysis and the quality controls applied to the ISS soundings (Miller 1994). The uncertainty in latent heating retrieved from SSM/I is about 20%. The error in radiative cooling rate could be as large as 10%–30%. Therefore, the worst-case uncertainty in estimated ver-

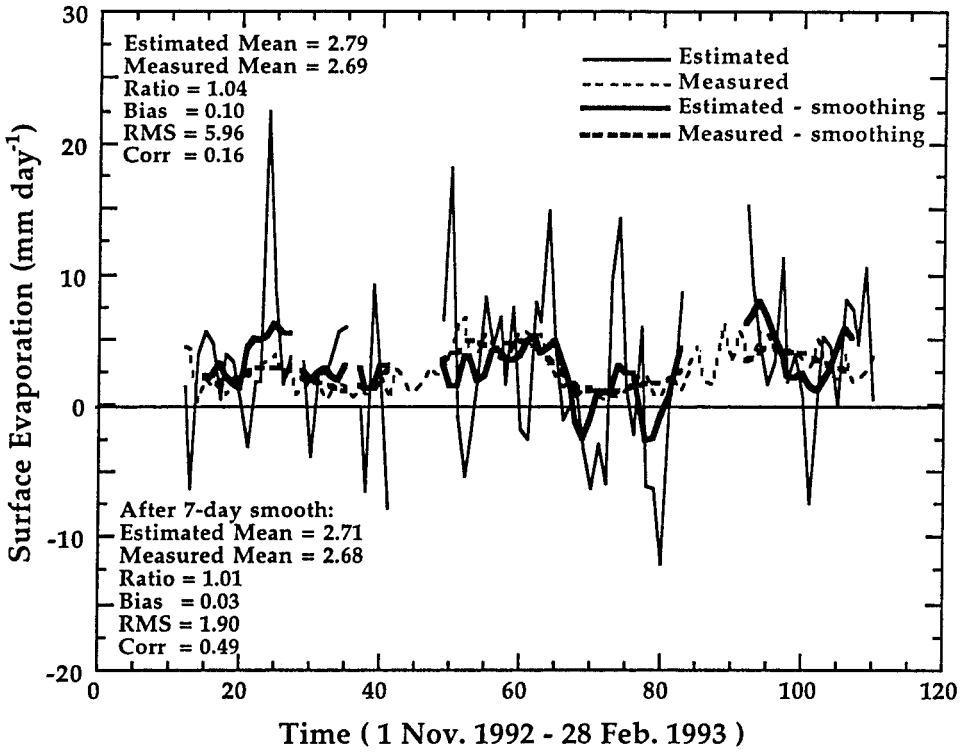

FIG. 15. Comparison of estimated and measured daily surface evaporation over IFA. Measured evaporation is calculated from bulk aerodynamic formula. Statistical parameters for nonsmoothed results are given in upper-left corner, and those for smoothed results are given in lower-left corner.

tical divergence (convergence) of eddy moisture (sensible heat) flux would be as large as 30%–50% but only if the assessed individual errors are noncorrelating and additive.

Last, it is important to recognize that the retrieved latent heating has more uncertainty in the lower troposphere because of reasons mentioned in section 4b. Thus, the estimated vertical eddy fluxes at low levels of the troposphere also are less certain. As evident from the comparisons with the Yanai et al. (1973), Esbensen and Wang (1988), and Gallus and Johnson (1991) results, however, the vertical structures of estimated vertical eddy fluxes for the middle and upper troposphere must be realistic. Therefore, the close agreement between the vertical integration of vertical divergence of eddy moisture flux with averaged surface evaporation bodes well for using the residual approach for investigating the role of turbulence in the heat–moisture budgets of convective–stratiform environments and in evaluating cloud parameterization techniques.

6. Conclusions

A total of 78 days of high-quality daily mean ISS sounding data from the TOGA COARE IOP and latent heating retrieved from SSM/I measurements were used for quantitatively investigating heat and moisture processes and large-scale Q_1–Q_2 budgets over IFA. The averaged vertical structures of heat and moisture are consistent with two other TOGA COARE studies by Frank and Wang (1996) and Lin and Johnson (1996), respectively, although the averaged magnitudes from Frank and Wang (1996) are larger because of different data processing and analysis schemes. The magnitude of rain-rate-normalized mean Q_1 within IFA is smaller than that found by Yanai et al. (1973) over the summer western Pacific area and yet close to that found over the SPCZ (e.g., Miller and Vincent 1987; Pedigo and Vincent 1990). The analysis of rain-rate-normalized mean Q_2 indicates that there is only one dominant drying peak near 550 hPa over IFA, but there are two separate peaks over the summer western Pacific (e.g., Yanai et al. 1973). These results suggest that convection is more active in boreal summer than in winter over the tropical western Pacific, which is consistent with its climatological rainfall nature in which December through May is the relative dry season.

When partitioned into convective and stratiform categories, the associated heating and moistening vertical structures are consistent with published results for different environments (e.g., Yanai et al. 1973; Houze 1982; Johnson 1984; Frank and McBride 1989). In general, there is positive heating throughout the troposphere, with a maximum amplitude near 425 hPa, with heating above and cooling below 600 hPa for convective and stratiform processes, respectively. There is drying

in most of the troposphere, with a maximum at 525 hPa for convective conditions, and drying above and moistening below 550 hPa for stratiform precipitation. Furthermore, the rain-rate-normalized mean Q_1 profiles have similar shapes and magnitudes for both convective and stratiform situations for different regions. The shapes and magnitudes of rain-rate-normalized Q_2 for stratiform conditions are also similar for various regions.

It is clearly evident that the large-scale Q_1–Q_2 budgets exhibit differences between mechanisms of heating and moistening processes for convective and stratiform situations, marked by layers in which the dominant term in the Q_1 budget for convection is not the dominant term for stratiform precipitation. For the Q_2 budget, the main difference is located in the 600–750-hPa layer, in which horizontal convergence dominates for convective environments, and vertical convergence dominates for stratiform environments.

The time series of mean tropospheric Q_1 and Q_2 exhibit a pronounced 20–30-day oscillation in which the active period is related to strong convection. Latent heating and Q_1 are closely related, with a correlation coefficient of 0.71 (at 1% significance level). The average magnitude of latent heating is about 70% of Q_1. In addition, large-scale horizontal convergence of moisture flux is correlated well with Q_1, with a correlation coefficient of 0.61 (also at 1% significance level) and a mean magnitude that represents about 61% of Q_1. These results demonstrate that the total heating of tropical systems mainly comes from latent heat release, with moisture balance depending on large-scale horizontal convergence of moisture flux.

The vertical divergence of vertical eddy moisture flux and vertical convergence of vertical eddy sensible heat flux have been explored using the retrieved latent heating from SSM/I measurements and diagnosed large-scale Q_1 and Q_2 calculations. The results show that cumulus-scale processes are important in the heat and moisture budgets. For example, the vertical divergence of eddy moisture flux exhibits different structures for convective and stratiform environments. For convective situations, cumulus-scale processes serve in the role of drying the middle troposphere while moistening the lower and upper troposphere. For stratiform conditions, such processes moisten the entire troposphere. Comparison with the model results of Tao et al. (1993) indicates that the main difference is found in the mid–lower troposphere. This finding likely stems from the fact that the Tao et al. results were averaged over the convective and stratiform regions of a squall line, and results of this study were averaged over the convective and stratiform elements of a larger area. These latter results have to be taken with some caution, because the estimated vertical convergence/divergence profiles of eddy sensible heat and moisture fluxes could have up to 30%–50% uncertainty stemming from various sources. Further improvements in the cloud-model simulations used for the retrieval algorithm and denser and higher-quality sounding measurements are needed to improve the retrieved latent heating profiles and the diagnosed turbulent fluxes of sensible heat and moisture.

Although the comparison between estimated daily surface evaporation (derived from the vertical integration of the vertical divergence of eddy moisture flux) and measured surface evaporation reveals uncertainties in the combined satellite–sounding analysis scheme, the systematic difference between estimates and observations is small. Here, it is important to note that the latter comparison is an independent quality check of the estimated eddy moisture flux using the residual between radiosonde-diagnosed Q_2 estimates and satellite-retrieved latent heating. The results suggest that the method presented here, used in a compositing framework, is applicable for investigating the role of turbulence in precipitating cloud systems, particularly strong convection, and for analyzing the performance of cloud parameterization schemes.

Acknowledgments. The authors thank Mr. Jimmy Merritt for his capable assistance in processing the SSM/I datasets. The surface rain gauge datasets were kindly provided by the Center for Ocean–Atmospheric Prediction Studies at The Florida State University under the directorship of Professor James J. O'Brien. This research has been supported by NSF Grant ATM-9300870 and NASA Grant NAGW-2672. A portion of the computing resources were provided by the Supercomputer Computation Research Institute at The Florida State University under U.S. Department of Energy Contract DOE-FC05-85ER250000.

APPENDIX

Terminal Velocities of Raindrops and Graupel Particles

a. Raindrops

The terminal velocity of raindrops is given by Pruppacher and Klett (1980):

$$W_{\mathrm{rd}} = \frac{\mathrm{Re}_{\mathrm{rd}}\eta}{\rho_a \overline{d}_{\mathrm{rd}}}, \tag{A1}$$

where η (kg m^{-1} s^{-1}) is expressed as

$$\eta = (1.718 + 0.0049T) \times 10^{-5} \quad T \geq 0°\mathrm{C} \quad \text{and} \tag{A2a}$$

$$\eta = (1.718 + 0.0049T - 1.2 \times 10^{-5} T^2) \times 10^{-5} \quad T < 0°\mathrm{C}. \tag{A2b}$$

It is assumed that the size distribution of raindrops $N(d)$ follows a Marshall and Palmer (1948) distribution, that is,

$$N(d) = n_o e^{-\lambda d}, \tag{A3}$$

where $n_o = 8 \times 10^6$ (m^{-4}), λ is a function of total rainwater, and d is the raindrop diameter. In addition, it is assumed that LWC is known, and that the raindrop diameters vary from d_1 to d_2. Therefore

$$\mathrm{LWC_{rd}} = \frac{\pi}{6}\rho_w \int_{d_1}^{d_2} d^3 N(d)\ \delta d$$

$$= \frac{\pi}{6\lambda^4}\rho_w n_o \{[(\lambda d_1)^3 + 3(\lambda d_1)^2 + 6\lambda d_1 + 6]e^{-\lambda d_1} - [(\lambda d_2)^3 + 3(\lambda d_2)^2 + 6\lambda d_2 + 6]e^{-\lambda d_2}\}, \quad \text{(A4)}$$

where ρ_w is liquid water density. The mass-weighted mean diameter of raindrops is given by

$$\overline{d_{\mathrm{rd}}} = \frac{\frac{\pi\rho_w}{6}\int_{d_1}^{d_2} d^4 N(d)\ \delta d}{\mathrm{LWC_{rd}}} = \frac{\pi\rho_w n_o}{6\mathrm{LWC_{rd}}}\frac{1}{\lambda^5}\{[(\lambda d_1)^4 + 4(\lambda d_1)^3 + 12(\lambda d_1)^2 + 24\lambda d_1 + 24]e^{-\lambda d_1}$$

$$- [(\lambda d_2)^4 + 4(\lambda d_2)^3 + 12(\lambda d_2)^2 + 24\lambda d_2 + 24]e^{-\lambda d_2}\}. \quad \text{(A5)}$$

If it is assumed further that d_1 and d_2 are respectively 0 and infinite, Eqs. (A4) and (A5) can be simplified as

$$\mathrm{LWC_{rd}} = \pi\rho_w n_o \lambda^{-4} \quad \text{(A6)}$$

$$\overline{d_{\mathrm{rd}}} = 4\lambda^{-1}. \quad \text{(A7)}$$

It is now clear that $\overline{d_{\mathrm{rd}}}$ can be estimated when $\mathrm{LWC_{rd}}$ is known. Note also that the results from Eqs. (A6) and (A7) are very close to those from Eqs. (A4) and (A5) when d_1 and d_2 are taken as 200 μm and 7 mm (i.e., the assumed characteristic magnitudes of the minimum and maximum sizes of raindrops). Therefore, Eqs. (A6) and (A7) are used in the current study. The terminal velocity can be calculated from Eq. (A1) once the Reynolds number is determined, as discussed below.

Because a raindrop is no longer considered to be spherical when its size is large, the Reynolds number of raindrops is different for small and large drops (Beard 1976). Therefore, the raindrops are divided into small and large groups according to size. The small group contains drops whose radius r is between 10 and 535 μm, and the large group contains drops whose r is between 535 μm and 3.5 mm.

1) GROUP 1: 10 $\mu\mathrm{m} \le r \le 535$ μm

The Davis or Best number $C_D\mathrm{Re_{rd}^2}$ is given by

$$C_D\mathrm{Re_{rd}^2} = \frac{4d^3(\rho_w - \rho_a)\rho_a g}{3\eta^2}, \quad \text{(A8)}$$

where C_D is the drag coefficient. Beard (1976) provides an empirical fit to describe the relationship between drag coefficients and Reynolds number, that is,

$$X = \ln(C_D\mathrm{Re_{rd}^2}) \quad \text{and} \quad \text{(A9a)}$$

$$\mathrm{Re_{rd}} = \exp\left(\sum_{i=0}^{6} B_i X^i\right), \quad \text{(A9b)}$$

where $B_0 = -0.318\,657 \times 10^{-1}$, $B_1 = 0.992\,696$, $B_2 = -0.153\,193 \times 10^{-2}$, $B_3 = -0.987\,059 \times 10^{-3}$, $B_4 = -0.578\,878 \times 10^{-3}$, $B_5 = 0.855\,176 \times 10^{-4}$, and $B_6 = -0.327\,815 \times 10^{-5}$. Thus, $\mathrm{Re_{rd}}$ can be estimated from Eqs. (A8) and (A9a), (A9b).

2) GROUP 2: 535 $\mu\mathrm{m} < r \le 3.5$ mm

Garner and Lihou (1965) found that W_{rd} of large-size raindrops depends on three independent dimensionless parameters. They are 1) Reynolds number $\mathrm{Re_{rd}} = 2rW_{\mathrm{rd}}\rho_a/\eta$, 2) Bond number $N_{\mathrm{Bo}} = g(\rho_w - \rho_a)r^2/\sigma$, and 3) "physical property" number $N_p = \sigma^3\rho_a^2/[\eta^4 g(\rho_w - \rho_a)]$. In these expressions, σ is the surface tension of water against air (dyn $\mathrm{cm^{-1}}$) expressed as $\sigma = 76.10 - 0.155\,T$, where T is temperature (°C). They also derived the function

$$N_{\mathrm{Bo}}N_p^{1/6} = F(N_p^{-1/6}\mathrm{Re_{rd}}). \quad \text{(A10)}$$

Beard (1976) specified this functional relationship from a fit to the experimental results of Gunn and Kinzer (1949) for water drops in air. He gives the following expressions:

$$Y = \sum_{i=0}^{5} B_i X^i, \tag{A11a}$$

$$X = \ln\left(\frac{16}{3} N_{\mathrm{Bo}} N_p^{1/6}\right), \tag{A11b}$$

$$Y = \ln(\mathrm{Re}_{\mathrm{rd}} N_p^{-1/6}), \quad \text{and} \tag{A11c}$$

$$\mathrm{Re}_{\mathrm{rd}} = N_p^{1/6} \exp(Y), \tag{A11d}$$

where $B_0 = -0.500\,015 \times 10^1$, $B_1 = 0.523\,778 \times 10^1$, $B_2 = -0.204\,914 \times 10^1$, $B_3 = 0.475\,294$, $B_4 = -0.542\,819 \times 10^{-1}$, and $B_5 = 0.238\,449 \times 10^{-2}$. Therefore, $\mathrm{Re}_{\mathrm{rd}}$ is estimated from Eqs. (A11a–A11d).

b. Graupel particles

The terminal velocity of graupel is given by Böhm (1989):

$$W_{\mathrm{ip}} = \frac{\mathrm{Re}_{\mathrm{ip}} \eta}{\rho_a \overline{d}_{\mathrm{ip}}}, \tag{A12a}$$

$$\mathrm{Re}_{\mathrm{ip}} = 8.5[(1 + 0.1519 X^{1/2})^{1/2} - 1]^2, \quad \text{and} \tag{A12b}$$

$$X = C_D \mathrm{Re}_{\mathrm{ip}}^2 = \frac{8 m g \rho_a}{\pi \eta^2}\left(\frac{A}{A_e}\right)^{1/4}, \tag{A12c}$$

where m is the graupel's mass. Furthermore, A_e is the effective projected area presented to the flow by the graupel, A is the area of the smallest circle or ellipse that completely contains A_e, and $(A/A_e)^{1/4}$ is the effect of graupel shape on terminal velocity. Böhm (1989) took a value of 0.95 as the shape parameter, whereas its value is 1.0 if the graupel is assumed to be spherical. Because the shape of an averaged graupel particle is considered to be spherical, we obtain

$$m = \frac{\pi}{6} \rho_{\mathrm{ip}} \overline{d}_{\mathrm{ip}}^{\,3}, \tag{A13}$$

where ρ_{ip} is the graupel density. Based on Kajikawa (1971), ρ_{ip} can be set to values of 420 and 230 kg m^{-3} for temperatures greater than/equal to or less than 0.5°C, respectively.

The size distribution of graupel particles, for diameters between 1 and 50 mm, is given by Auer (1972) as

$$N_{\mathrm{ip}}(d) = 561.3 d^{-3.4}, \tag{A14}$$

where the units of N_{ip} and d are m^{-3} mm^{-1} and mm, respectively. It is assumed that the minimum diameter of graupel is 1 mm and the diameters vary from d_1 to d_2. Therefore, the equivalent liquid water content $\mathrm{LWC}_{\mathrm{ip}}$ of graupel is given by

$$\mathrm{LWC}_{\mathrm{ip}} = \frac{\pi}{6} \rho_{\mathrm{ip}} \int_{d_1}^{d_2} d^3 N_{\mathrm{ip}}(d)\, \delta d. \tag{A15}$$

When the units of $\mathrm{LWC}_{\mathrm{ip}}$ and d are taken as g m^{-3} and mm, Eq. (A15) can be reexpressed as

$$d_2 = \exp\left[\frac{\ln(2041.5386 \mathrm{LWC}_{\mathrm{ip}} + 1)}{0.6}\right]. \tag{A16}$$

The mass-weighted, averaged diameter of graupel is then given by

$$\overline{d}_{\mathrm{ip}} = \frac{\frac{\pi \rho_{\mathrm{ip}}}{6} \int_{d_1}^{d_2} d^4 N_{\mathrm{ip}}(d)\, \delta d}{\mathrm{LWC}_{\mathrm{ip}}} = 1.836\,85 \times 10^{-4}\, \rho_{\mathrm{ip}} (d_2^{1.6} - 1)/\mathrm{LWC}_{\mathrm{ip}}. \tag{A17}$$

REFERENCES

Ackerman, S. A., and S. K. Cox, 1987: Radiative energy budget estimates for the 1979 southwest summer monsoon. *J. Atmos. Sci.,* **44,** 3052–3078.

Adler, R. F., A. J. Negri, P. R. Keehn, and I. M. Hakkarinen, 1993: Estimation of monthly rainfall over Japan and surrounding waters from a combination of low-orbit microwave and geosynchronous IR data. *J. Appl. Meteor.*, **32,** 335–356.

Auer, A. H., Jr., 1972: Distribution of graupel and hail with size. *Mon. Wea. Rev.*, **100,** 325–328.

Beard, K. V., 1976: Terminal velocity and shape of cloud and precipitation drops aloft. *J. Atmos. Sci.*, **33,** 851–864.

Bell, G. D., and A. N. Basist, 1994: Seasonal climate summary. The global climate of December 1992–February 1993. Part I: Warm ENSO conditions continue in the tropical Pacific; California drought abates. *J. Climate*, **7,** 1581–1605.

Böhm, H. P., 1989: A general equation for the terminal fall speed of solid hydrometeors. *J. Atmos. Sci.*, **46,** 2419–2427.

Bradley, E. F., P. A. Coppin, and J. S. Godfrey, 1991: Measurements of sensible and latent heat flux in the western equatorial Pacific ocean. *J. Geophys. Res.*, **96,** 3375–3389.

Cox, S. K., and K. T. Griffith, 1979: Estimates of radiative divergence during Phase III of the GARP Atlantic Tropical Experiment. Part II: Analysis of Phase III results. *J. Atmos. Sci.*, **36,** 586–601.

Dopplick, T. G., 1972: Radiative heating of the global atmosphere. *J. Atmos. Sci.*, **29,** 1278–1294.

Ebert, E. E., 1996: Results of the 3rd Algorithm Intercomparison Project (AIP-3) of the Global Precipitation Climatology Project (GPCP). BMRC Research Rep. 55, 199 pp. [Available from Bureau of Meteorology Research Centre, GPO Box 1289K, Melbourne, Victoria 3000, Australia.]

——, and M. J. Manton, 1998: Performance of satellite rainfall estimation algorithms during TOGA COARE. *J. Atmos. Sci.*, **55,** 1537–1557.

Esbensen, S. K., and J. T. Wang, 1988: A composite life cycle of nonsquall mesoscale convective systems over the tropical ocean. Part II: Heat and moisture budgets. *J. Atmos. Sci.*, **45,** 537–548.

Farrar, M. R., and E. A. Smith, 1992: Spatial resolution enhancement of terrestrial features using deconvolved SSM/I microwave brightness temperatures. *IEEE Trans. Geosci. Remote Sens.*, **30,** 349–355.

——, ——, and X. Xiang, 1994: The impact of spatial resolution enhancement of SSM/I microwave brightness temperatures on rainfall retrieval algorithms. *J. Appl. Meteor.*, **33,** 313–333.

Frank, W. M., and J. L. McBride, 1989: The vertical distribution of heating in AMEX and GATE cloud clusters. *J. Atmos. Sci.*, **46,** 3464–3478.

——, and H. Wang, 1996: Rawinsonde budget analyses during the TOGA COARE. *J. Atmos. Sci.*, **53,** 1761–1780.

Gallus, W. A., Jr., and R. H. Johnson, 1991: Heat and moisture budgets of an intense midlatitude squall line. *J. Atmos. Sci.*, **48,** 122–146.

Garner, F. H., and D. A. Lihou, 1965: Mass transfer to and from drops in gaseous streams. *DECHEMA Monogr.*, **55,** 155–178.

Gunn, R., and G. D. Kinzer, 1949: The terminal velocity of fall for water drops in stagnant air. *J. Meteor.,* **6,** 243–248.
Gutzler, D. S., G. N. Kiladis, G. A. Meehl, K. M. Weickmann, and M. Wheeler, 1994: Seasonal climate summary. The global climate of December 1992–February 1993. Part II: Large-scale variability across the tropical western Pacific during TOGA COARE. *J. Climate,* **7,** 1606–1622.
Hartmann, D. L., H. H. Hendon, and R. A. Houze Jr., 1984: Some implications of the mesoscale circulations in tropical cloud clusters for large-scale dynamics and climate. *J. Atmos. Sci.,* **41,** 113–121.
Houze, R. A., Jr., 1982: Cloud clusters and large-scale vertical motions in the tropics. *J. Meteor. Soc. Japan,* **60,** 396–410.
——, 1989: Observed structure of mesoscale convective systems and implications for large-scale heating. *Quart. J. Roy. Meteor. Soc.,* **115,** 427–461.
——, and E. N. Rappaport, 1984: Air motions and precipitation structure of an early summer squall line over the eastern tropical Atlantic. *J. Atmos. Sci.,* **41,** 553–574.
Johnson, R. H., 1976: The role of convective-scale precipitation downdrafts in cumulus and synoptic-scale interactions. *J. Atmos. Sci.,* **33,** 1890–1910.
——, 1984: Partitioning tropical heat and moisture budgets into cumulus and mesoscale components: Implications for cumulus parameterization. *Mon. Wea. Rev.,* **112,** 1590–1600.
Kajikawa, M., 1971: A model experimental study on the falling velocity of ice crystals. *J. Meteor. Soc. Japan,* **49,** 367–375.
Katayama, A., 1967: On the radiation budget of the troposphere over the Northern Hemisphere (III): Zonal cross-sections and energy considerations. *J. Meteor. Soc. Japan,* **45,** 26–38.
Kummerow, C., and L. Giglio, 1994a: A passive microwave technique for estimating rainfall and vertical structure information from space. Part I: Algorithm description. *J. Appl. Meteor.,* **33,** 3–18.
——, and ——, 1994b: A passive microwave technique for estimating rainfall and vertical structure information from space. Part II: Applications to SSM/I data. *J. Appl. Meteor.,* **33,** 19–34.
——, W. S. Olson, and L. Giglio, 1996: A simplified scheme for obtaining precipitation and vertical hydrometeor profiles from passive microwave sensors. *IEEE Trans. Geosci. Remote Sens.,* **34,** 1213–1232.
——, W. Barnes, T. Kozu, J. Shiue, and J. Simpson, 1998: The tropical rainfall measuring mission (TRMM) sensor package. *J. Atmos. Oceanic Technol.,* **15,** 809–817.
Lau, K. M., and L. Peng, 1987: Origin of low-frequency (intraseasonal) oscillations in the tropical atmosphere. Part I: Basic theory. *J. Atmos. Sci.,* **44,** 950–972.
Lin, X., and R. H. Johnson, 1996: Heating, moistening, and rainfall over the western Pacific warm pool during TOGA COARE. *J. Atmos. Sci.,* **53,** 3367–3383.
Marshall, J. S., and W. M. Palmer, 1948: The distribution or raindrops with size. *J. Meteor.,* **5,** 165–166.
McBride, J. L., and G. Holland, 1989: The Australia Monsoon Experiment (AMEX): Early results. *Aust. Meteor. Mag.,* **37,** 23–35.
——, N. E. Davidson, K. Puri, and G. C. Tyrell, 1995: The flow during TOGA COARE as diagnosed by the BMRC tropical analysis and prediction system. *Mon. Wea. Rev.,* **123,** 717–736.
Miller, B. I., 1962: On the momentum and energy balance of hurricane Helene (1958). National Hurricane Research Project, Rep. 53, U.S. Weather Bureau, Washington, DC, 19 pp.
Miller, B. L., and D. G. Vincent, 1987: Convective heating and precipitation estimates for the tropical South Pacific during FGGE, 10–18 January 1979. *Quart. J. Roy. Meteor. Soc.,* **113,** 189–212.
Miller, E., 1994: TOGA COARE Integrated Sounding System Data Report. Vols. 1–9, 799 pp. [Available from Surface and Sounding Systems Facility, NCAR, P.O. Box 3000, Boulder, CO 80307.]
Palmén, E., and H. Riehl, 1957: Budget of angular momentum and energy in tropical cyclones. *J. Meteor.,* **14,** 150–159.
Parsons, D. B., and Coauthors, 1994: The Integrated Sounding System: Description and preliminary observations from TOGA COARE. *Bull. Amer. Meteor. Soc.,* **75,** 553–567.
Pedigo, C. B., and D. G. Vincent, 1990: Tropical precipitation rates during SOP-1, FGGE, estimated from heat and moisture budgets. *Mon. Wea. Rev.,* **118,** 542–557.
Pruppacher, H. R., and J. P. Klett, 1980: *Microphysics of Clouds and Precipitation.* Reidel, 714 pp.
Rasmusson, E. M., and T. H. Carpenter, 1982: Variations in tropical sea surface temperature and surface wind fields associated with the Southern Oscillation/El Niño. *Mon. Wea. Rev.,* **110,** 354–384.
Riehl, H., and J. S. Malkus, 1958: On the heat balance in the equatorial trough zone. *Geophysica,* **6,** 503–538.
Schaack, T. K., D. R. Johnson, and M.-Y. Wei, 1990: The three-dimensional distribution of atmospheric heating during the GWE. *Tellus,* **42A,** 305–327.
Short, D. A., P. A. Kucera, B. S. Ferrier, J. C. Gerlach, S. A. Rutledge, and O. W. Thiele, 1997: Shipboard radar rainfall patterns within the TOGA COARE IFA. *Bull. Amer. Meteor. Soc.,* **78,** 2817–2836.
Simpson, J., C. Kummerow, W.-K. Tao, and R. F. Adler, 1996: On the Tropical Rainfall Measuring Mission (TRMM) satellite. *Meteor. Atmos. Phys.,* **60,** 19–36.
Smith, E. A., X. Xiang, A. Mugnai, and G. J. Tripoli, 1994a: Design of an inversion-based precipitation profile retrieval algorithm using an explicit cloud model for initial guess microphysics. *Meteor. Atmos. Phys.,* **54,** 53–78.
——, A. Mugnai, and G. Tripoli, 1994b: Theoretical foundations and verification of a multispectral, inversion-type microwave precipitation profile retrieval algorithm. *Proceedings of the ESA/NASA International Workshop on Microwave Radiometry,* VSP Science Press, 599–621.
——, C. Kummerow, and A. Mugnai, 1994c: The emergence of inversion-type precipitation profile algorithms for estimation of precipitation from satellite microwave measurements. *Remote Sens. Rev.,* **11,** 211–242.
——, X. Xiang, A. Mugnai, R. E. Hood, and R. W. Spencer, 1994d: Behavior of an inversion-based precipitation retrieval algorithm with high-resolution AMPR measurements including a low-frequency 10.7-GHz channel. *J. Atmos. Oceanic Technol.,* **11,** 858–873.
——, and Coauthors, 1998: Results of WetNet PIP-2 project. *J. Atmos. Sci.,* **55,** 1483–1536.
Tao, W.-K., J. Simpson, C.-H. Sui, B. Ferrier, S. Lang, J. Scala, M.-D. Chou, and K. Pickering, 1993: Heating, moisture, and water budgets of tropical and midlatitude squall lines: Comparisons and sensitivity to longwave radiation. *J. Atmos. Sci.,* **50,** 673–690.
Thompson, R. M., S. W. Payne, E. E. Recker, and R. J. Reed, 1979: Structure of synoptic-scale wave disturbances in the intertropical convergence zone of the eastern Atlantic Ocean. *J. Atmos. Sci.,* **36,** 53–71.
Tripoli, G. J., 1992: A nonhydrostatic model designed to simulate scale interaction. *Mon. Wea. Rev.,* **120,** 1342–1359.
Wilheit, T., and Coauthors, 1994: Algorithms for the retrieval of rainfall from passive microwave measurements. *Remote Sens. Rev.,* **11,** 163–194.
Wu, D.-H., D. L. Anderson, and M. K. Davey, 1993: ENSO variability and external impacts. *J. Climate,* **6,** 1703–1717.
Yanai, M., and T. Tomita, 1998: Seasonal and interannual variability of atmospheric heat sources and moisture sinks as determined from NCEP–NCAR reanalysis. *J. Climate,* **11,** 463–482.
——, S. Esbensen, and J. H. Chu, 1973: Determination of bulk properties of tropical cloud clusters from large-scale heat and moisture budgets. *J. Atmos. Sci.,* **30,** 611–627.
Yang, S., and E. A. Smith, 1999a: Moisture budget analysis of TOGA COARE area using SSM/I-retrieved latent heating and large-scale Q_2 estimates. *J. Atmos. Oceanic Technol.,* **16,** 633–655.
——, and ——, 1999b: Four-dimensional structure of monthly latent heating derived from SSM/I satellite measurements. *J. Climate,* **12,** 1016–1037.